

Iberian hydroclimate variability and the Azores High during the last 1200 years: evidence from proxy records and climate model simulations

Received: 22 March 2021 / Accepted: 18 July 2022 © The Author(s), under exclusive licence to Springer-Verlag GmbH Germany, part of Springer Nature 2022

Abstract

The state of the atmospheric circulation and the associated hydroclimate in the North Atlantic during the last millennium remain the subject of considerable debate in both proxy- and model-based studies. Of particular interest in the Iberian region is the Azores High (AH) system, the southern node of the North Atlantic Oscillation (NAO), an atmospheric dipole closely tied to regional hydroclimate. Hydroclimate-sensitive proxy reconstructions from this region offer some insights into atmospheric dynamics, but large spatiotemporal gaps in these data inhibit a robust evaluation of hydroclimate variability. In this study, we present a continuous, sub-decadally-resolved composite stalagmite carbon isotopic record from three partially overlapping stalagmites from Buraca Gloriosa (BG) cave, western Portugal, situated within the center of the AH, that preserves evidence of regional hydroclimate variability from approximately 800 CE to the present. Chronologies are derived from U/Th dating and annual laminae. Stalagmite carbon isotopic values primarily reflect the amount of effective moisture and reveal generally dry conditions during the Medieval Climate Anomaly (MCA; ~850-1250 CE) and Modern Climate/ Industrial Era (1850 CE-present), and wetter conditions during the Little Ice Age (LIA; ~1400–1850 CE). Multidecadal to centennial variability in the BG record and state-of-the-art last millennium climate model simulations show considerable coherence with precipitation-sensitive records from Spain and Morocco that, like BG, are strongly influenced by the intensity, size, and location of the AH. Model-proxy synthesis suggests that western Portugal was persistently dry during much of the MCA consistent with other NAO reconstructions; however, even considering age uncertainties, the apparent timing in the transition from a relatively dry MCA to a wetter LIA is spatially variable and confirms the non-stationary behavior of the AH system indicated by model output.

Keywords Stalagmite · Azores High · Hydroclimate · Last millennium · Last Millennium Ensemble · Paleoclimate

1 Introduction

Proxy reconstructions along Iberia and western Europe generally show distinct hydroclimate regimes over the past millennium, most notably those associated with the Medieval

Climate Anomaly (MCA; ~850–1250 CE), the Little Ice Age (LIA; ~1400–1850 CE), and the Modern Climate (1850 CE-present; e.g., Cook et al. 2015; Trouet et al. 2009). Many records from southwest Europe (Iberia) and northwest Africa (Morocco) indicate drier conditions during the MCA

☐ Diana L. Thatcher thatcher@iastate.edu

Published online: 16 August 2022

- Department of Geological and Atmospheric Sciences, Iowa State University, Ames, IA, USA
- Department of Geology, Cornell College, Mt. Vernon, IA, USA
- Department of Physical Oceanography, Woods Hole Oceanographic Institution, Woods Hole, MA, USA

- Department of Earth and Planetary Sciences, University of New Mexico, Albuquerque, NM, USA
- Kansas Geological Survey, University of Kansas, Lawrence, KS, USA
- Department of Anthropology, University of Louisville, Louisville, KY, USA
- Department of Geosciences, Union College, Schenectady, NY, USA



compared to the LIA, while the opposite is true for more northern sites (e.g., Scotland) (see Baker et al. 2011; Baker et al. 2015; Cook et al. 2015; Esper et al. 2007; Moreno et al. 2012; Ramos-Román et al. 2016; Sánchez-López et al. 2016; Trouet et al. 2009). However, consensus has not yet been reached on whether these hydroclimate dynamics were primarily related to external factors such as volcanic aerosols or solar luminosity or were driven, instead, by internal variability within the climate system. The North Atlantic Oscillation (NAO) and the Azores High (AH) pressure system are important parameters to consider when evaluating the causes of hydroclimate variability in this region.

The AH subtropical pressure system comprises the southern node of the NAO dipole and is related to the subsidence associated with the descending limb of the Hadley circulation, which gives rise to the aridity of the Mediterranean region, including the Iberian Peninsula (Karnauskas and Ummerhofer 2014; Seidel et al. 2008). Typically, the NAO index is defined as the sea level pressure (SLP) difference between Iceland and the Azores or Lisbon, Portugal (Barnston and Livezey 1987) (Fig. 1). The NAO is considered the dominant mode of climate variability in the North Atlantic region, especially during winter (Barnston and Livezey 1987; Hurrell 1995; Trigo et al. 2004, 2005; van Loon and Rogers 1978). The winter NAO index is usually only considers DJFM, however, the wettest time period in Mediterranean climates spans fall through spring (Rüdisühli et al. 2020; Trigo et al. 2005). Although the intensity, size, and location of the AH control the hydroclimate of the Iberian Peninsula by influencing storms tracks (Fig. 1), the dynamics of the AH are poorly constrained through space and time (Iqbal et al. 2013; Karnauskas and Ummerhofer 2014; Wallace and Hobbs, 2006). Reconstructions of the AH system are critical for accurately evaluating Iberian hydroclimate variability; however it has been more common to consider the NAO system as a whole. To evaluate whether regional hydroclimate is largely tied to AH/NAO dynamics during recent centuries to millennia, integrated proxy- and model-based studies are necessary to reach beyond the short historical records of the NAO that extend only to 1864 CE (Hurrell 1995).

Numerous reconstructions of the NAO have been developed, but the most widely cited is that of Trouet et al. (2009). By coupling growth laminae in a Scottish stalagmite record (Baker et al. 2011; Proctor et al. 2000) with a Moroccan tree ring record (Esper et al. 2007) (see Fig. 1), both of which represent proxies for precipitation, these authors reconstructed the mean state of the winter NAO (wNAO; for the months of DJFM) since 1049 CE. Based on a modern calibration between this combined record and an instrumental measure of the wNAO index, Trouet et al. (2009) argued that during medieval times the NAO was in a persistently positive state (intensified low pressure over Iceland, intensified high pressure over the Azores from ~ 1060-1440 CE). Following on this work, Ait Brahim et al. (2017) used a stalagmite δ^{18} O record from Ifoulki cave in southwestern Morocco to describe NAO and precipitation variability over the last millennium. The findings of this study indicate prevailing

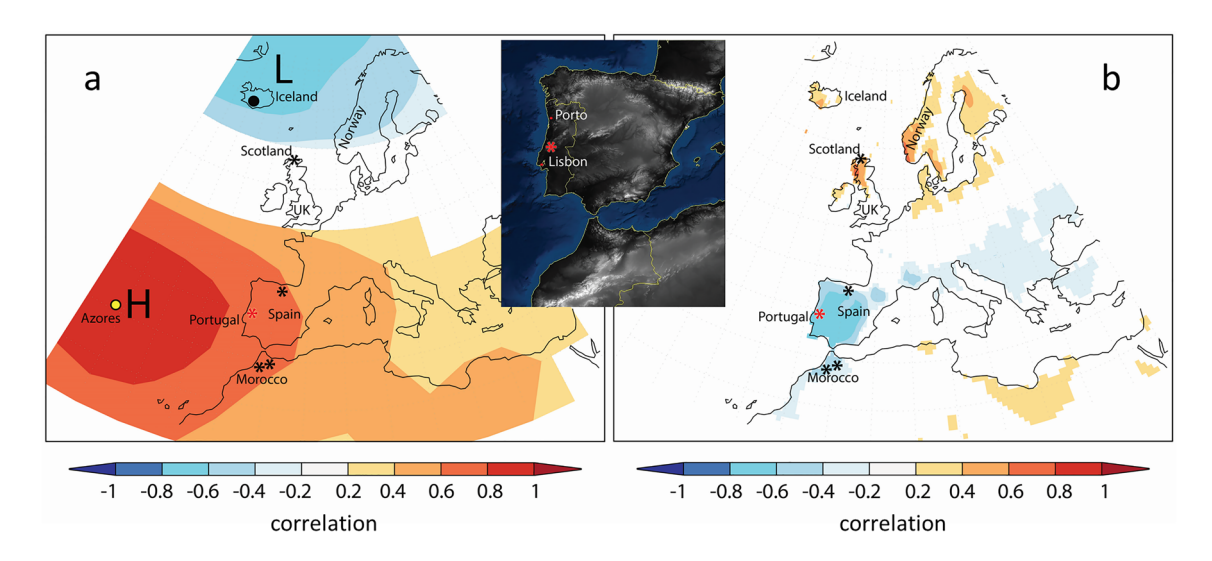


Fig. 1 Regional setting of study area. **a** Azores sea-level pressure (SLP) correlated with SLP from the North Atlantic region (1899–1997) for December, January, February, March (winter NAO time period) and **b** Azores SLP correlated with winter (DJFM) precipitation in the region (1901–2014). Note high level of negative correlation in western Portugal indicating higher Azores SLP is correlated with lower amounts of precipitation. Maps adapted from

KNMI Climate Explorer (http://climexp.knmi.nl/). Azores SLP data (DJFM 1866–1997) from Ponta Delgada, Azores. Regional SLP data (1899-present) Trenberth and Paolino (1980). Regional precipitation data from CRU TS3.23 (1901–2014) with 0.5° grid size. Black asterisks indicate proxy records discussed in this manuscript—Scotland (Baker et al. 2015), Spain (Martín-Chivelet et al. 2011) and Morocco (Ait Brahim et al. 2018; Esper et al. 2007; Wassenburg et al. 2013)



dry conditions during the MCA (defined as 900–1350 CE), a pluvial period after 1400 CE with wetter conditions over the latter part of the LIA (centered ~ 1680 CE and ~ 1810 CE) and drying conditions towards modern times. Somewhat complicating direct links to the NAO, the climate of southwestern Morocco appears to be sensitive to both the NAO and the Atlantic Multidecadal Oscillation (Ait Brahim et al. 2017). The results from Ait Brahim et al. (2017) are partially contradicted by a reconstruction of NAO variability derived from 97 tree-ring series from the Euro-Mediterranean region by Cook et al. (2019) that does not indicate a persistently positive NAO over the MCA. In fact, this record details a slightly negative NAO between 1090 and 1300 CE.

Behavior of the wNAO at its northern node (similar to the Scotland record in Trouet et al. 2009; Fig. 1) has been examined through a sediment record from a central Norwegian fjord. Faust et al. (2016) estimated the behavior of the NAO over the past 2800 years based on primary productivity indicators that are largely influenced by precipitation effects during the winter. They found a positive NAO state for much of the MCA (defined there as 950-1200 CE) that apparently strengthened through time with a rapid shift to NAO negative conditions around 1250 CE. However, the shift to an NAO negative mode in central Norway appears to have preceded the changes noted by Trouet et al. (2009) by about two centuries. Faust et al. (2016) further suggested that the wNAO was primarily in a negative mode until about 1750 CE with the NAO oscillating between positive and negative modes since that time. Additional studies have investigated the variability of the NAO system during the Common Era (Baker et al. 2015; Hernández et al. 2020; Luterbacher et al. 2001; Olsen et al. 2012; Ortega et al. 2015; Sjolte et al. 2018).

These additional proxy-based NAO records, coupled with climate model simulations, provide important tests of the Trouet et al. (2009) NAO reconstruction. For example, dry conditions would have been entrenched across much of the western Mediterranean if the NAO system was in a persistently positive state for much of the MCA, as proposed by Trouet et al. (2009; Fig. 1) and indicated from several records in the Sánchez-López (2016) Iberian Peninsula compilation. However, other proxy records from the region provide evidence of wet intervals during the MCA in Iberia (Martín-Chivelet et al. 2011; Moreno et al. 2012) and Morocco (Wassenburg et al. 2013). Additionally, modeling studies have not been able to replicate the persistently positive NAO conditions during the MCA (Lehner et al. 2012; Ortega et al. 2015).

One potential issue with the Trouet et al. (2009) NAO reconstruction is the location of the Moroccan tree ring records at the southern node (Fig. 1), because the non-stationary behavior of the southern NAO dipole may have reduced the ability of some proxy records to capture changes

in the intensity of the NAO system (Comas-Bru and McDermott 2014; López-Moreno and Vicente-Serrano 2008; Raible et al. 2014; Schmutz et al. 2000). Besides changes in atmospheric circulation and precipitation dynamics that could be associated with changes in the mean state of the NAO (Hurrell 1995), relatively little attention has been given to atmospheric dynamics, namely the intensity, size, and location (see Wassenburg et al. 2016) of the AH, the subtropical high system marking the southern node of the NAO, in driving hydroclimate across the western Mediterranean.

In this study we developed a hydroclimate-sensitive stalagmite composite δ^{13} C record from western Portugal, a site located within the AH (southern node of the NAO system). Changes in stalagmite δ^{13} C values in this region are primarily driven by precipitation changes that modulate local vegetation densities (Thatcher et al. 2020b), both of which are highly coupled to the behavior of the AH. By pairing these data with output from the Last Millennium Ensemble (LME) of the Community Earth System Model (CESM1; Otto-Bliesner et al. 2015), we explored the behavior (intensity, size, and location) of the AH for the last ~ 1200 years. Integrating these new model and proxy data with previously published high-resolution precipitation proxy records that have strong age controls from Spain and Morocco (Ait Brahim et al. 2018; Esper et al. 2007; Martín-Chivelet et al. 2011; Trouet et al. 2009; Wassenburg et al. 2013) allowed us to determine the regional coherence of these precipitationsensitive proxy records and to test the behavior of the AH as a possible mechanism for explaining regional hydroclimate variations within and between these records.

2 Dynamics of the Azores High

The location of the AH is linked to the Hadley circulation, where the equatorward (rising) branch of the Hadley circulation coincides with the Intertropical Convergence Zone (ITCZ), and the descending limb with the subtropical high pressure belt, including the AH. Poleward/equatorward shifts in the ITCZ as the rising branch of the Hadley Circulation could be associated with concomitant latitudinal shifts in the location of the AH, altering the patterns of hydroclimate in Iberia and the rest of the Mediterranean region (Seidel et al. 2008). For example, if the boreal summer ITCZ shifted southward during the LIA as suggested by several studies (Brönnimann et al. 2015; Haug et al. 2001; Schneider et al. 2014), then western Iberia would have become wetter as the AH also moved equatorward (Iqbal et al. 2013). Others have suggested that, at times, the ITCZ has both expanded and weakened or contracted and intensified (Asmerom et al. 2020). Without adequate spatial coverage, a southern migration of the ITCZ could be incorrectly interpreted at some sites as a weakening of the AH. Similarly, contraction of the



Hadley cell (e.g., Tandon et al. 2013) would potentially have the same effect on the hydroclimate of Portugal. Projections in climate models suggest increasing dryness in the Mediterranean region (including Iberia) that is consistent with changes in Hadley cell circulation and a shifting/expanding subtropical high in the twenty-first century (IPCC 2013).

The intensity, size, and location of AH can vary substantially over time (Davis et al. 1997). In recent decades, the intensity of the AH has strengthened (particularly in January), and due to its impact on regional weather and climate, it is important to constrain variations in the AH pressure field as well as latitudinal and longitudinal changes (Falarz 2019; Iqbal et al. 2013). Variability in the AH has far-reaching effects, impacting northwest Europe's precipitation with latitudinal shifts (Rashid et al. 2012) and the influence of the NAO on precipitation of the Middle East is primarily through changes in the strength of the AH (Iqbal et al. 2013). Recent variability in the location of the center of action of the AH has been documented by Falarz (2019) who found that the winter AH has shifted slightly westward and southward since 1945 CE.

In concert with modeling attempts, another feasible way to deconvolve potential non-stationary effects of the AH through time is to establish a network of high-quality, precipitation-sensitive proxy records that are situated in the zone of influence of the AH system, including those zones that would be affected by migration of the AH. Extending the time range over which we can accurately reconstruct the AH pressure system will provide useful context for future climate scenarios. This is the goal of this study.

3 Study area and methods

3.1 Cave and environmental monitoring

Buraca Gloriosa (BG) cave is located in western Portugal in the zone of influence of the AH (see Denniston et al. 2018 and Thatcher et al. 2020a for a detailed description of this cave system). The regional climate exhibits a strong inverse relationship between regional SLP (the strength of the AH) and precipitation (Fig. 1). Rainfall is highly seasonal, with the majority occurring between October and April (~85% in Leiria, 30 km from BG). A strong AH serves to block storms from reaching Iberia, steering them towards northern Europe and diminishing rainfall across Portugal. Conversely, when the AH weakens, storm tracks originating from the Atlantic shift south, and western Iberia experiences increased rainfall (Raible et al. 2004). Western Portugal is thus an ideal location to study the long-term behavior of the AH and NAO because its location at the southern edge of the storm tracks associated with mid-latitude westerlies. This positioning also makes it highly sensitive to NAO dynamics (Moreno et al. 2011).

BG is a small cave (about $40 \times 10 \times 15$ m; 39° 32' N, 08° 47' W; 420 m a.s.l.) located within the Estremadura Limestone Massif (Rodrigues and Fonseca 2010) roughly 20 km from the Atlantic Ocean (Fig. 1). The cave has only one small (approx. 0.5 m²) entrance, sheltered at the base of a cliff and behind a large wall of collapsed boulders with dense tree cover that shields the entrance from wind and sunlight and severely restricts air flow. Shrubs, small trees, and mosses dominate the vegetation above the cave, and the soil layer is thin (< 10 cm) and highly organic. Environmental data including atmospheric pressure, temperature, and relative humidity collected both inside and outside the cave documented conditions over a ~8.5-year period (Thatcher et al. 2020a; also Fig. S1). Drip count data were collected for ~7.5 years using Stalagmate acoustic drip counters (Collister and Mattey 2008; Thatcher et al. 2020a). Three cylindrical and active calcite stalagmites (BG131, BG134, BG136; 19.6 cm, 9.7 cm, and 43.7 cm, respectively; Fig. S2) were collected ~ 30 m from the entrance (420 m a.s.l.). All three stalagmites were collected in 2013 from BG cave and were inspected visually. Stalagmites BG131, BG134, and BG136 were found to be composed of clear to milky calcite with a minimum of detritus; a change to denser, more optically translucent calcite occurs near the top of each (Fig. S2). Fluorescent laminae were identified in the stalagmites as described below.

3.2 Age model

For dating of the three stalagmites, approximately 100-150 mg of calcite was milled parallel to growth layers, dissolved, spiked with a mixed ²²⁹Th-²³³U-²³⁶U tracer, and processed according to chemical separation methods of Asmerom et al. (2010). The U and Th isotopes were measured using a Thermo-Neptune multi-collector inductively coupled plasma mass spectrometer (MC-ICP-MS) at the University of New Mexico Radiogenic Isotope Laboratory. ^{233}U and ^{236}U and ^{232}Th were measured with $10^{12}~\Omega$ resistors, while ^{235}U and ^{238}U with $10^{11}~\Omega$ and $10^{10}~\Omega$ resistors on Faraday cups respectively. ²³⁴U and ²³⁰Th were measured on a secondary electron multiplier (SEM) that sits behind a high-abundance filter. All measurements were done on static mode. Standards NBL-112 and an in-house ²³⁰Th-²²⁹Th solution were analyzed several times during the run sessions to accurately establish the gain between the SEM and Faraday cups. An initial 230 Th/ 232 Th ratio value of 13.5 ± 6.75 ppm was assigned to these samples based on analysis of modern drip water and an isochron at 109 mm from the stalagmite top. Despite this independent control on unsupported ²³⁰Th, as well as the active growth apparent on the stalagmite cap, it was unclear if deposition had been continuous throughout



the last century because of somewhat large age uncertainties related to low uranium abundances (Table 1). Therefore, as an additional constraint on recent stalagmite deposition, we milled one approximately 15 mg sample from the uppermost portion of BG136 for radiocarbon analysis at the National Ocean Sciences Accelerator Mass Spectrometry (NOSAMS) facility at Woods Hole Oceanographic Institution. Rather than a direct radiometric age, this sample was used detect the mid-twentieth century atmospheric ¹⁴C anomaly ("bombpeak") to confirm recent stalagmite deposition.

To further constrain the age models and to develop a composite record, stable isotope ratios from each of the three stalagmites were integrated using intra-site correlation age modelling (iscam; Fohlmeister 2012), iscam provides an objective method for combining records, reduces age uncertainty, and yields a quantitative assessment of the coherence between discrete time series (Griffiths et al. 2016). Using the parameters of 2000 pairs of artificially simulated first order autoregressive time series (AR1) and 100,000 Monte Carlo simulations, and with a 30-year smoothing, and using the δ^{13} C records for each stalagmite, the highest correlation between the four portions of the stalagmites (BG131, BG134, and portions both above and below a hiatus in BG136) within allowable age uncertainties using a point-wise linear interpolation between adjacent U-Th dates was determined. Z-scores of δ^{13} C values were placed on the highest correlation age models for the individual stalagmite portions to create the composite carbon isotope record that was compared to other regional records and NAO reconstructions.

To test the reliability of the age models of the individual components of the record generated with iscam, additional age modelling software was used. StalAge (Scholz and Hoffman 2011) utilizes a multiple step approach where major outliers are identified, then minor outliers and age inversions are identified, and finally the age model and 95% confidence windows are created using Monte Carlo simulations. StalAge creates the age model and uncertainty by fitting straight lines to subsets of the age data. Constructing Proxy Records from Age Models (COPRA) also uses Monte Carlo simulations to determine the final age models and 95% confidence windows but uses piecewise cubic Hermite interpolation (Breitenbach et al. 2012). COPRA also determines a 95% confidence window for the proxy record as well as the age model.

Age models were supplemented using fluorescent lamina counting. Stalagmite BG136 was imaged using a Leica SP5 X MP confocal/multiphoton microscope system with an inverted microscope front end in the Roy J. Carver High Resolution Microscopy Facility at Iowa State University. Excitation and emission wavelengths were 405 nm and 416–790 nm, respectively. Additionally, stalagmite BG136 was imaged using an Olympus

BX53 paired with an X-Cite fluorescent light source and FITC filter with excitation and emission wavelengths of 467–498 nm and 512–556 nm, respectively. Laminae were counted and measured five times above a hiatus (Fig. S3) in BG136 and the average of these values was used, with differences in the final count propagated as an uncertainty error. Stalagmites BG131 and BG134 were also imaged but inconsistent laminae in these two samples led us to focus solely on BG136 for this aspect of the chronology.

3.3 Carbon isotopic values

All stable isotope measurements were performed at the Stable Isotope Laboratory at Iowa State University. Stalagmite BG136 was sectioned lengthwise using a water-cooled trim saw, polished, and micromilled at 200 µm resolution for the top 100 mm along the central growth axis for carbon isotopes using a computer-guided Mercantek micromill. Stalagmites BG134 and BG131 were prepared in a similar manner but sampled at 50 µm resolution to account for much slower growth rates compared to BG136. They were micromilled over the top 35.45 mm (BG134) and 6.3 mm (BG131) along the central growth axis. δ^{13} C isotope ratios on stalagmite samples were measured using a Thermo Finnegan Delta Plus XL spectrometer coupled with a Gas Bench II and CombiPal autosampler. Based on isotopic standards (NBS-19, NBS-18) the average analytical uncertainty across multiple runs was $\pm 0.08\%$ (1 σ , VPDB) for δ^{13} C values. Oxygen isotopes for these stalagmites were also measured and are presented in Fig. S4a.

As reported by Thatcher et al. (2020b), stalagmite δ¹³C values from in this location primarily reflect precipitation amounts. Furthermore, Thatcher et al. (2020b) argued a close coupling between precipitation amounts and vegetation densities. As precipitation in the region increased, vegetation also increased and the stalagmite carbon isotopic values decreased reflecting the inputs from vegetation and soil processes (Denniston et al. 2018; Thatcher et al. 2020b). Conversely, when precipitation was lower, vegetation also decreased and the carbon isotopic values increased reflecting less of a vegetation/soil influence and more of a rock influence.

Since ~1840 CE, carbon isotope values from terrestrial and marine records have decreased towards the present in response to the increase in atmospheric CO_2 derived from burning of fossil fuels, which have nominal $\delta^{13}C$ values around -27% (e.g., Sharp 2007). This Suess Effect (Keeling 1979) has impacted other carbon-rich paleorecords in terrestrial and marine environments (e.g. Druffel and Benavides, 1986; Railsback et al. 2018; Schöne et al. 2011; Swart et al. 2010; Verburg 2007). The carbon composite



Table 1 U-Th isotopic ratios and ²³⁰Th ages

BG136 4.5 8.0 1.6 28.7 1.3 0.0042 0.0013 4.8 2.3 3.5 1.1 2.5 BG136 4 9.0 4 9.0 4.0 9.0 1.3 0.0023 1.6 1.7 9.0 1.0 2.0 2.0 1.2 1.0 1.0 1.2 1.0 1.2 1.0 1.2 1.0 1.2 1.0 1.2 1.0 1.0 1.2 1.0 1.0 1.2 1.0 1.0 1.2 1.0 1.0 1.2 1.0 1.2 1.0 1.0 1.2 1.0 <td< th=""><th>Stalagmite</th><th>Distance to top (mm)</th><th>238U (ng g⁻¹)</th><th>232Th (pg g⁻¹)</th><th>6234U (corrected)</th><th>Error</th><th>230Th/238U (activity)</th><th>Error</th><th>230Th/232Th (ppm)</th><th>Error</th><th>Uncorrected age (Yr BP)^a</th><th>Error (yr)</th><th>Corrected age (Yr BP)^b</th><th>Error (yr)^c</th></td<>	Stalagmite	Distance to top (mm)	238U (ng g ⁻¹)	232Th (pg g ⁻¹)	6234U (corrected)	Error	230Th/238U (activity)	Error	230Th/232Th (ppm)	Error	Uncorrected age (Yr BP) ^a	Error (yr)	Corrected age (Yr BP) ^b	Error (yr) ^c
4 900 4.0 29.7 1.3 0.0029 0.0012 103 111 249 103 7 1000 4.0 315.3 1.3 0.0065 0.00124 144 93 539 104 17 100.0 4.40 315.3 1.3 0.0065 20.7 1.0 1.0 2.2 1.4 9.3 539 104 1.0	BG136	2.5	80.0	116.0	287.7	1.3	0.0042	0.00135	48	23	353	114	253	129
7 100.0 74.0 315.3 1.3 0.065 0.00124 144 93 53.9 104 12.7 60.7 45.4 1.4 0.0071 0.00120 56 17 58.9 104 12.7 45.8 445.8 1.4 0.0071 1.0 7 57.5 103 13.5 45.8 45.8 1.4 0.0078 0.00120 1.7 57.5 103 21.5 79.0 85.0 351.4 1.4 0.0088 0.00121 1.8 7.2 7.9 103 25.3 79.0 85.0 34.5 1.4 0.0088 0.00121 4.8 7.9 103 29.5 79.0 188.0 34.5 1.4 0.0169 35.2 1.2 7.9 17.2 1.2 29.5 79.0 188.0 1.4 0.0179 0.0015 4.7 7.0 1.7 1.7 1.7 1.7 1.7 1.7 1.7 1.7 <td>BG136</td> <td>4</td> <td>0.06</td> <td>42.0</td> <td>292.7</td> <td>1.3</td> <td>0.0029</td> <td>0.00122</td> <td>103</td> <td>1111</td> <td>249</td> <td>103</td> <td>216</td> <td>109</td>	BG136	4	0.06	42.0	292.7	1.3	0.0029	0.00122	103	1111	249	103	216	109
127 101.7 213.7 345.4 1.4 0,0071 0,00130 56 17 581 106 172 183.5 458.8 349.5 1.4 0,0071 0,0013 228 217 575 103 172 183.6 458.8 349.5 1.4 0,008 0,00123 228 217 575 103 215 64.0 490 346.5 1.4 0,0018 229 194 942 125 194 942 152 25.3 64.0 490 346.5 1.4 0,0149 0,0013 28 194 942 125 194 942 125 194 942 125 125 143 0,0149 0,0013 188 125 126 0,0149 0,0013 88 194 141 942 125 125 125 0,0149 0,0013 189 125 125 126 0,0149 0,013 149 141 141 <td>BG136</td> <td>7</td> <td>100.0</td> <td>74.0</td> <td>315.3</td> <td>1.3</td> <td>0.0065</td> <td>0.00124</td> <td>144</td> <td>93</td> <td>539</td> <td>104</td> <td>489</td> <td>1111</td>	BG136	7	100.0	74.0	315.3	1.3	0.0065	0.00124	144	93	539	104	489	1111
172 89.5 45.8 349.5 14 0,0071 0.0012 28 217 575 103 19 113.0 840.0 840.0 140.0 345.3 1.4 0,008 0,00121 118 48 716 99 215 790 85.0 345.0 1.4 0,016 0,0013 189 48 716 99 25.3 732 64.0 49.0 345.0 1.4 0,016 0,013 189 77 176 99 29.5 79.0 188.0 324.5 1.4 0,016 0,0013 28 179 175 175 175 175 175 175 175 175 175 175 175 175 175 175 175 175 178 176 175 175 178 178 179 175 178 178 179 175 178 178 179 179 175 178 179	BG136	12.7	101.7	213.7	345.4	1.4	0.0071	0.00130	56	17	581	106	441	131
19 113.0 140.0 345.3 14 0.0088 0.00121 118 48 716 99 21.5 79.0 85.0 351.4 1.4 0.0088 0.00153 149 82 792 155 25.3 64.0 85.0 346.5 1.4 0.016 0.00153 189 82 170 175 125 29.5 79.0 188.0 324.5 1.6 0.0140 0.00153 98 27 155 125 39 82.0 46.0 312.8 1.4 0.0140 0.00153 189 27 160 125 40 188.0 174.0 26.1 1.4 0.0167 0.00152 13 124 13 0.0294 0.00153 141 141 141 141 0.0167 0.00152 13 141 141 141 141 141 141 141 141 141 141 141 141 141 141	BG136	17.2	89.5	45.8	349.5	1.4	0.0071	0.00127	228	217	575	103	541	109
21.5 79.0 85.0 351.4 1.4 0,008 0,001.3 149 82 79.2 125 25.3 64.0 49.0 346.5 1.4 0,016 0,001.9 25.2 194 942 125 25.3 73.2 66.5 34.5 1.4 0,015 0,001.8 88 190 77 1160 125 39. 78.0 188.0 324.5 1.4 0,015 0,001.8 49 7.5 112 39. 108.0 174.0 296.1 1.4 0,015 0,001.8 49 7.5 112 40. 188.0 174.0 296.1 1.4 0,016 0,011.3 49 41.3 96 67.5 88.0 173.0 252.0 284.6 1.3 0,029 0,001.3 49 25 118 6.5 88.0 1710 36.2 1.3 0,026 0,011.3 41 27 175 118	BG136	19	113.0	140.0	345.3	1.4	0.0088	0.00121	118	48	716	66	634	1111
25 64,0 49.0 346.5 1.4 0.0116 0.00149 252 194 942 122 25.3 73.2 69.5 343.0 1.4 0.010 0.00153 288 130 976 125 29.5 79.0 188.0 324.5 1.6 0.0140 0.00153 457 50 115 125 39 82.0 46.0 312.8 1.4 0.017 0.00159 457 50 125 60 188.0 174.0 296.1 1.4 0.017 0.00159 457 50 113 134 60 7.8 10.2 174.0 206.1 1.4 0.017 0.0015 173 173 113 134 <td< td=""><td>BG136</td><td>21.5</td><td>79.0</td><td>85.0</td><td>351.4</td><td>1.4</td><td>0.0098</td><td>0.00153</td><td>149</td><td>82</td><td>792</td><td>125</td><td>720</td><td>135</td></td<>	BG136	21.5	79.0	85.0	351.4	1.4	0.0098	0.00153	149	82	792	125	720	135
25.3 73.2 69.5 343.0 1.4 0.0120 0.00153 28 130 976 125 29.5 79.0 188.0 324.5 1.6 0.0440 0.00153 98 27 1160 127 39 82.0 46.0 312.8 1.4 0.0147 0.00153 487 503 1311 134 50 108.0 174.0 296.1 1.4 0.0167 0.00153 139 27 1413 96 60 78.0 123.0 225.5 1.3 0.0204 0.00153 136 143 196 176 118 60 78.0 123.0 286 1.3 0.0204 0.00153 136 178 118 95 88.0 171.0 36.2 1.3 0.0204 0.00123 136 127 179 118 112 88.0 171.0 3142 1.3 0.0204 0.00123 18 271 <td< td=""><td>BG136</td><td>25</td><td>64.0</td><td>49.0</td><td>346.5</td><td>1.4</td><td>0.0116</td><td>0.00149</td><td>252</td><td>194</td><td>942</td><td>122</td><td>891</td><td>130</td></td<>	BG136	25	64.0	49.0	346.5	1.4	0.0116	0.00149	252	194	942	122	891	130
29.5 79.0 188.0 324.5 1.6 0.0140 0.00153 457 1160 127 39 82.0 46.0 312.8 1.4 0.0157 0.00159 457 503 1311 134 50 188.0 174.0 296.1 1.4 0.0157 0.0015 457 503 1311 134 66.5 18.0 123.0 275.5 1.3 0.0204 0.00153 136 224 118 96 66.5 87.0 220.0 286.6 1.3 0.0209 0.00123 81 2249 118 85 96.0 196.0 286.6 1.3 0.0209 0.00123 81 2249 106 95 88.0 171.0 314.2 1.5 0.023 0.0018 27 2713 109 112 152.0 88.2 1.3 0.023 0.0018 27 2713 109 112 16.4 0.033	BG136	25.3	73.2	69.5	343.0	1.4	0.0120	0.00153	208	130	926	125	913	135
39 82.0 46.0 312.8 1.4 0.0157 0.00159 457 503 1311 134 50 108.0 174.0 296.1 1.4 0.0167 0.00112 171 49 1413 96 60 78.0 123.0 275.5 1.3 0.0204 0.0013 136 172 178 18 67.5 87.0 220.0 283.4 1.3 0.0209 0.0013 136 179 118 96 85 96.0 196.0 306.2 1.3 0.0262 0.0012 179 179 176 112 152.0 88.2 134.2 1.5 0.023 0.0018 2249 107 107 112 152.0 68.2 135.0 1.4 0.032 0.0018 147 107 107 2 13.2 14.0 0.032 0.0164 14 177 179 2 14.9 14.4 0.0146 <td>BG136</td> <td>29.5</td> <td>79.0</td> <td>188.0</td> <td>324.5</td> <td>1.6</td> <td>0.0140</td> <td>0.00153</td> <td>86</td> <td>27</td> <td>1160</td> <td>127</td> <td>1001</td> <td>155</td>	BG136	29.5	79.0	188.0	324.5	1.6	0.0140	0.00153	86	27	1160	127	1001	155
50 108.0 174.0 296.1 1.4 0.0167 0.00112 171 49 1413 96 60 78.0 123.0 255.5 1.3 0.0204 0.0013 136 22 1757 118 60.5 87.0 220.0 283.4 1.3 0.020 0.00123 81 8 1790 106 85 96.0 196.0 286.6 1.3 0.020 0.0013 81 8 1790 106 95 88.0 171.0 346.2 1.3 0.026 0.0119 249 56 2597 107 112 18.0 171.0 314.2 1.5 0.033 0.0018 277 7 179 107 0.8 91.9 116.0 31.2 1.4 0.0048 0.0018 4 2 73 10 10 1 104.9 116.1 34.4 1.4 0.0048 0.0015 14 11 <t< td=""><td>BG136</td><td>39</td><td>82.0</td><td>46.0</td><td>312.8</td><td>1.4</td><td>0.0157</td><td>0.00159</td><td>457</td><td>503</td><td>1311</td><td>134</td><td>1272</td><td>141</td></t<>	BG136	39	82.0	46.0	312.8	1.4	0.0157	0.00159	457	503	1311	134	1272	141
60 78.0 123.0 275.5 1.3 0.0204 0.00135 213 72 1757 118 67.5 87.0 220.0 283.4 1.3 0.0209 0.00123 136 28 1790 106 73 89.0 475.0 286.6 1.3 0.0262 0.00123 81 8 2249 106 85 96.0 196.0 306.2 1.3 0.0202 0.00123 81 1790 106 95 88.0 171.0 314.2 1.3 0.0262 0.00124 24 52597 107 0.8 18.0 171.0 314.2 1.3 0.0048 0.0018 77 73 102 0.8 1.3 1.4 0.0048 0.0016 4 2 73 101 0.8 1.04.9 1.176.7 3.64.9 3.5 0.0146 0.0022 18 73 101 1. 1.04.9 3.4 0.00	BG136	50	108.0	174.0	296.1	1.4	0.0167	0.00112	171	49	1413	96	1302	115
67.5 87.0 220.0 283.4 1.3 0.0209 0.00133 136 28 1790 106 73 89.0 475.0 286.6 1.3 0.0262 0.00123 81 8 1790 106 85 96.0 196.0 366.2 1.3 0.0328 0.00193 87 259 107 95 88.0 171.0 314.2 1.5 0.0323 0.00186 277 72 2713 109 112 152.0 68.2 35.5 1.8 0.032 0.00186 172 72 2713 109 0.8 91.9 164.0 33.4 0.048 0.00186 14 4 21 4 27 73 109 109 1.4 117.1 36.1 1.4 0.0146 0.00126 14 2 73 73 11 101 101 101 101 101 101 101 101 101 10	BG136	09	78.0	123.0	275.5	1.3	0.0204	0.00135	213	72	1757	118	1647	135
73 89.0 475.0 286.6 1.3 0.0262 0.00123 81 8 2249 107 85 96.0 196.0 306.2 1.3 0.0368 0.00119 249 56 2597 107 95 88.0 171.0 314.2 1.5 0.0323 0.0018 277 72 2713 109 112 152.0 68.2 325.9 1.8 0.0323 0.0018 277 72 2713 109 0.8 91.9 164.0 393.0 1.8 0.0018 277 72 2713 109 2 104.9 1176.7 376.3 1.4 0.0048 0.0016 4 2 738 101 8 79.7 82.1 36.3 1.4 0.0146 0.0022 199 4 177 179 9 66.5 147.8 36.4 1.4 0.0146 0.0022 199 4 177 179 <td>BG136</td> <td>67.5</td> <td>87.0</td> <td>220.0</td> <td>283.4</td> <td>1.3</td> <td>0.0209</td> <td>0.00123</td> <td>136</td> <td>28</td> <td>1790</td> <td>106</td> <td>1615</td> <td>142</td>	BG136	67.5	87.0	220.0	283.4	1.3	0.0209	0.00123	136	28	1790	106	1615	142
85 96.0 196.0 306.2 1.3 0.0308 0.00119 249 56 2597 102 95 88.0 171.0 314.2 1.5 0.0323 0.0018 277 72 2713 109 112 152.0 68.2 35.9 1.8 0.032 0.0018 120 1887 2770 157 109 0.8 91.9 164.0 393.0 3.4 0.048 0.018 27 77 109 109 2 104.9 1176.7 376.3 1.4 0.009 144 2 738 101 9 66.5 147.8 363.1 1.4 0.014 0.0022 109 41 177 179 17 90.3 157.7 364.9 3.5 0.0146 0.0022 109 47 140 101 18 95.3 102.2 2.4 0.022 0.00148 154 29 2173 119 <td>BG136</td> <td>73</td> <td>0.68</td> <td>475.0</td> <td>286.6</td> <td>1.3</td> <td>0.0262</td> <td>0.00123</td> <td>81</td> <td>∞</td> <td>2249</td> <td>107</td> <td>1879</td> <td>215</td>	BG136	73	0.68	475.0	286.6	1.3	0.0262	0.00123	81	∞	2249	107	1879	215
95 88.0 171.0 314.2 1.5 0.032 0.00186 277 72 2713 109 112 152.0 68.2 325.9 1.8 0.032 0.00186 120 1887 2770 157 0.8 91.9 164.0 393.0 3.4 0.0048 0.00167 44 21 376 137 2 104.9 1176.7 376.3 1.4 0.0016 0.00126 14 2 738 101 9 66.5 147.8 363.1 1.4 0.014 0.0022 109 41 177 179 17 90.3 147.8 364.9 3.5 0.0146 0.0022 109 41 177 179 17 90.3 157.7 376.4 1.4 0.0146 0.0022 109 47 179 179 18 101.7 296.4 382.0 2.4 0.0222 0.0018 15 179 179 <td>BG136</td> <td>85</td> <td>0.96</td> <td>196.0</td> <td>306.2</td> <td>1.3</td> <td>0.0308</td> <td>0.00119</td> <td>249</td> <td>99</td> <td>2597</td> <td>102</td> <td>2458</td> <td>127</td>	BG136	85	0.96	196.0	306.2	1.3	0.0308	0.00119	249	99	2597	102	2458	127
112 152.0 68.2 325.9 1.8 0.033 0.00186 120 1887 2770 157 0.8 91.9 164.0 393.0 3.4 0.0048 0.00167 44 21 376 132 2 104.9 1176.7 376.3 1.4 0.0049 0.00156 14 2 738 101 8 79.7 82.1 364.9 3.5 0.0146 0.00072 166 915 78 9 66.5 147.8 364.9 3.5 0.0146 0.0022 109 41 177 179 17 90.3 157.7 376.4 1.4 0.0175 0.00126 182 47 1400 101 29 101.7 296.4 382.0 2.4 0.0272 0.00148 154 176 197 119 28 102.2 397.8 1.4 0.0250 0.0019 176 176 177 197 <t< td=""><td>BG136</td><td>95</td><td>88.0</td><td>171.0</td><td>314.2</td><td>1.5</td><td>0.0323</td><td>0.00128</td><td>277</td><td>72</td><td>2713</td><td>109</td><td>2582</td><td>131</td></t<>	BG136	95	88.0	171.0	314.2	1.5	0.0323	0.00128	277	72	2713	109	2582	131
0.8 91.9 164.0 393.0 3.4 0.0048 0.00166 44 21 376 132 2 104.9 1176.7 376.3 1.4 0.0093 0.00126 14 2 738 101 8 79.7 82.1 363.1 1.4 0.0014 0.00097 166 66 915 78 101 9 66.5 147.8 364.9 3.5 0.0146 0.0022 109 41 1177 179 17 90.3 157.7 376.4 1.4 0.0175 0.00126 182 47 140 179 29 101.7 296.4 382.0 2.4 0.0272 0.00148 154 29 173 119 31 95.3 102.2 397.8 1.4 0.0250 0.0013 385 176 197 105 2.8 193.2 545.3 1.5 0.0026 0.0016 15 16 19	BG136	112	152.0	68.2	325.9	1.8	0.0332	0.00186	1220	1887	2770	157	2740	165
2 104.9 1176.7 376.3 1.4 0.0093 0.00126 14 2 738 101 8 79.7 82.1 363.1 1.4 0.014 0.00097 166 66 915 78 9 66.5 147.8 364.9 3.5 0.0146 0.0022 109 41 1177 179 17 90.3 157.7 376.4 1.4 0.0175 0.00126 182 47 1400 101 29 101.7 296.4 382.0 2.4 0.0175 0.00148 154 1400 101 31 95.3 102.2 397.8 1.4 0.0250 0.00132 385 176 197 105 2.8 193.2 545.3 499.3 1.6 0.0026 0.00106 57 9 709 73 73 3.4 190.6 123.3 493.4 1.5 0.0110 0.0069 3400 165 709<	BG134	8.0	91.9	164.0	393.0	3.4	0.0048	0.00167	44	21	376	132	262	148
8 79.7 82.1 363.1 1.4 0.0114 0.00097 166 66 915 78 9 66.5 147.8 364.9 3.5 0.0146 0.00222 109 41 1177 179 17 90.3 157.7 376.4 1.4 0.0175 0.00126 182 47 1400 101 29 101.7 296.4 382.0 2.4 0.0272 0.00148 154 29 2173 119 9.5 101.7 296.4 382.0 2.4 0.0250 0.00132 385 176 197 105 0.5 149.7 2010.9 547.2 2.0 0.0126 0.0019 1 890 65 2.8 193.2 445.3 1.5 0.0078 0.00100 57 9 709 73 3.4 19.6 13.5 481.3 1.5 0.0110 0.00069 3400 1955 812 51	BG134	2	104.9	1176.7	376.3	1.4	0.0093	0.00126	14	2	738	101	8	379
9 66.5 147.8 364.9 3.5 0.0146 0.00222 109 41 1177 179 17 90.3 157.7 376.4 1.4 0.0175 0.00126 182 47 1400 101 29 101.7 296.4 382.0 2.4 0.0272 0.00148 154 29 2173 119 0.5 101.7 296.4 382.0 2.4 0.0250 0.00132 385 176 197 105 0.5 149.7 2010.9 547.2 2.0 0.0126 0.0091 15 19 30 47 30 2.8 193.2 545.3 493.4 1.5 0.0078 0.00106 57 9 709 73 31 4.7 253.9 13.5 481.3 1.5 0.0110 0.00069 3400 1955 812 51 6 201.5 310.1 640.3 1.9 0.0159 0.00108 <t< td=""><td>BG134</td><td>∞</td><td>79.7</td><td>82.1</td><td>363.1</td><td>1.4</td><td>0.0114</td><td>0.00097</td><td>166</td><td>99</td><td>915</td><td>78</td><td>847</td><td>88</td></t<>	BG134	∞	79.7	82.1	363.1	1.4	0.0114	0.00097	166	99	915	78	847	88
17 90.3 157.7 376.4 1.4 0.0175 0.00126 182 47 1400 101 29 101.7 296.4 382.0 2.4 0.0272 0.00148 154 29 2173 119 31 95.3 102.2 397.8 1.4 0.0250 0.00132 385 176 1971 105 0.5 149.7 2010.9 547.2 2.0 0.0126 0.00191 15 1 890 65 2.8 193.2 545.3 499.3 1.6 0.0097 0.00106 57 9 709 73 5 3.4 190.6 123.3 493.4 1.5 0.0110 0.00064 198 76 569 47 5 4.7 253.9 13.5 481.3 1.5 0.0110 0.00069 3400 1955 812 51 8 6 201.5 310.1 60159 0.0169 0.00168 1	BG134	6	66.5	147.8	364.9	3.5	0.0146	0.00222	109	41	1177	179	1032	199
1 29 101.7 296.4 382.0 2.4 0.0272 0.00148 154 29 2173 119 1 31 95.3 102.2 397.8 1.4 0.0250 0.00132 385 176 1971 119 1 0.5 149.7 2010.9 547.2 2.0 0.0126 0.00091 15 1 890 65 1 2.8 193.2 545.3 499.3 1.6 0.0078 0.00100 57 9 709 73 5 3.4 190.6 123.3 493.4 1.5 0.0110 0.00064 198 76 569 47 5 4.7 253.9 13.5 481.3 1.5 0.0110 0.00069 3400 1955 812 51 8 6 201.5 310.1 640.3 1.9 0.0159 0.00168 170 39 1063 73 9	BG134	17	90.3	157.7	376.4	1.4	0.0175	0.00126	182	47	1400	101	1287	120
4 31 95.3 102.2 397.8 1.4 0.0250 0.00132 385 176 1971 105 1 0.5 149.7 2010.9 547.2 2.0 0.0126 0.00091 15 1 890 65 1 2.8 193.2 545.3 499.3 1.6 0.0097 0.00100 57 9 709 73 5 3.4 190.6 123.3 493.4 1.5 0.0110 0.00069 3400 1955 812 51 8 4.7 253.9 13.5 481.3 1.5 0.0110 0.00169 3400 1955 812 51 8 6 201.5 310.1 640.3 1.9 0.0159 0.00168 170 39 1063 73 9	BG134	29	101.7	296.4	382.0	2.4	0.0272	0.00148	154	29	2173	119	1985	155
0.5 149.7 2010.9 547.2 2.0 0.0126 0.00091 15 1 890 65 1 2.8 193.2 545.3 499.3 1.6 0.0097 0.00100 57 9 709 73 73 3.4 190.6 123.3 493.4 1.5 0.0178 0.00064 198 76 569 47 13 4.7 253.9 13.5 481.3 1.5 0.0110 0.00069 3400 1955 812 51 9 6 201.5 310.1 640.3 1.9 0.0159 0.00108 170 39 1063 73 9	BG134	31	95.3	102.2	397.8	1.4	0.0250	0.00132	385	176	1971	105	1902	114
1 2.8 193.2 545.3 499.3 1.6 0.0007 0.00100 57 9 709 73 3.4 190.6 123.3 493.4 1.5 0.0078 0.00064 198 76 569 47 4.7 253.9 13.5 481.3 1.5 0.0110 0.00069 3400 1955 812 51 6 201.5 310.1 640.3 1.9 0.0159 0.00108 170 39 1063 73	BG131	0.5	149.7	2010.9	547.2	2.0	0.0126	0.00091	15	1	068	65	1111	393
3.4 190.6 123.3 493.4 1.5 0.0078 0.00064 198 76 569 47 4.7 253.9 13.5 481.3 1.5 0.0110 0.00069 3400 1955 812 51 6 201.5 310.1 640.3 1.9 0.0159 0.00108 170 39 1063 73	BG131	2.8	193.2	545.3	499.3	1.6	0.0097	0.00100	57	6	402	73	543	112
4.7 253.9 13.5 481.3 1.5 0.0110 0.00069 3400 1955 812 51 6 201.5 310.1 640.3 1.9 0.0159 0.00108 170 39 1063 73	BG131	3.4	190.6	123.3	493.4	1.5	0.0078	0.00064	198	92	569	47	530	53
6 201.5 310.1 640.3 1.9 0.0159 0.00108 170 39 1063 73	BG131	4.7	253.9	13.5	481.3	1.5	0.0110	0.00069	3400	1955	812	51	813	53
	BG131	9	201.5	310.1	640.3	1.9	0.0159	0.00108	170	39	1063	73	626	98

U-Th isotopic ratios and ²³⁰Th ages

^aPresent defined as the year 2013 CE

^bInitial ²³⁰Th/²³²Th atomic ratio of 13.5 (±6.75) ppm used to correct for unsupported ²³⁰Th in BG stalagmites

^cErrors at 2σ level. Decay constants used: $\lambda_{230} = 9.1705$ e-6/yr; $\lambda_{234} = 2.82206$ e-6/yr; $\lambda_{238} = 1.55125$ e-10/yr (Cheng et al. 2013)



record after ~ 1840 CE from BG cave has thus been corrected according to the methods of Railsback et al. (2018) and Verburg (2007).

3.4 Community Earth System Model (CESM1)

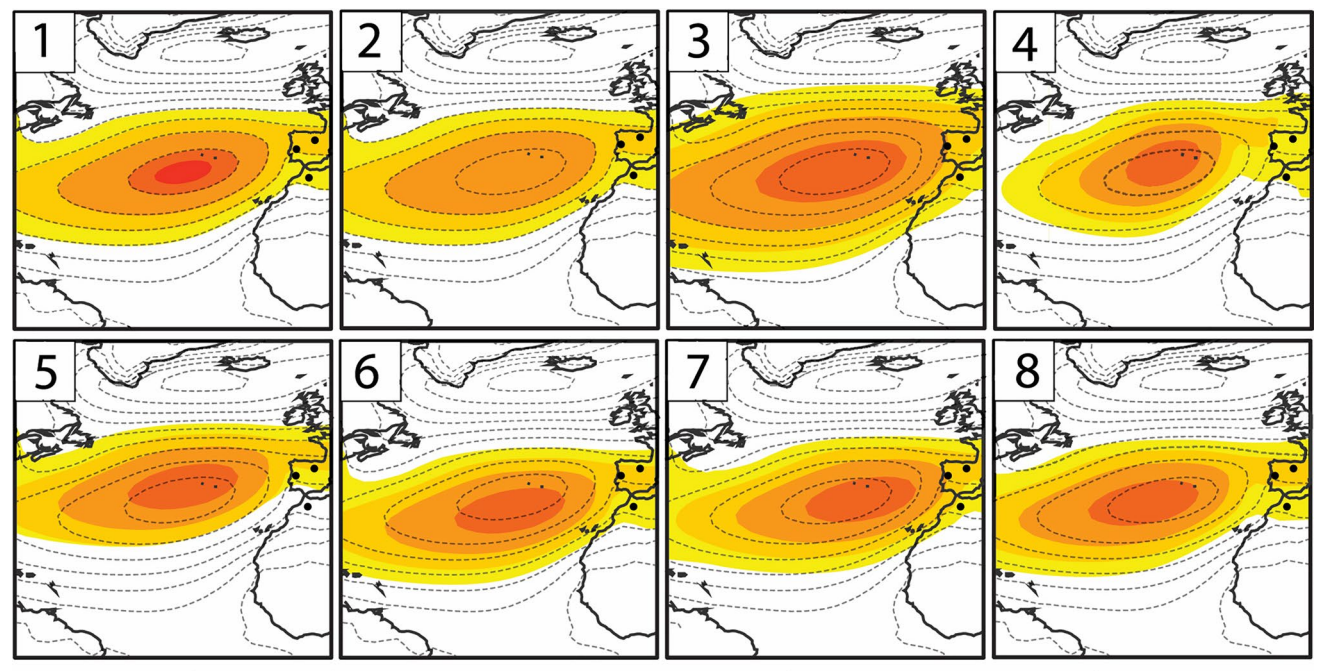
The Community Earth System Model (CESM1) was developed by the National Center for Atmospheric Research (NCAR) and is a fully-coupled, global climate model providing simulations of the past, present, and future climate states. A series of last millennium experiments, called the Last Millennium Ensemble (LME; Otto-Bliesner et al. 2015), were conducted by the CESM1 Paleoclimate Working Group at NCAR. The LME covers the time period 850 to 2006 CE and consists of 30 ensemble members. Thirteen of them consist of full transient forcing (e.g., greenhouse gas, aerosol, land-use, orbital, solar, volcanic). All model fields shown in this study are based on the multi-ensemble mean for all available 13 fully forced ensemble members.

The LME was used to assess the behavior of the winter AH (DJF). The LME climate model SLP results indicate changes in intensity, size, and location of the AH during the last 1200 years. The AH is defined here as the region of the North Atlantic which has a seasonally-averaged SLP above 1018.5 hPa, though results are similar when employing an objective SLP threshold as in Cresswell-Clay et al. (2022).

The center of mass of the AH was used to define the most extreme eastern, western, northern, or southern positions (in °N or °E). The strength of the AH was defined using the area-averaged seasonal SLP in the AH and the anomalous large and small spatial coverage AH years were determined by the area (in km²) of the region above 1018.5 hPa (methods adapted from Cresswell-Clay et al. 2022). Additionally, the impacts on regional SLP anomalies, moisture transport anomalies, and precipitation anomalies were determined for each set of extreme attributes (i.e. the top 10% of winter with extremely eastern position or the top 10% of winters with extremely southern position). A schematic depicting the possible scenarios for AH behavior that were investigated in this study are shown in Fig. 2. The extreme 10% of each of eight attributes (e.g. strong, weak, large, small, north, south, west, east) were determined and frequencies of each attribute per 100 years were calculated.

3.5 Observational and reanalysis products

Several global gridded observational and reanalysis products were used to validate the LME climate model simulations. At monthly resolution, the following datasets were used: HadSLP2r by the UK Hadley Centre at 5° horizontal resolution and available for the period 1850-present (Allan and Ansell 2006), 20th Century Reanalysis version 2 (20CR)



1. Strengthen 2. Weaken 3. Expand 4. Contract 5. Shift north 6. Shift south 7. Shift east 8. Shift west

Fig. 2 LME model output mean deviation types of the Azores High. Schematic representation of spatiotemporal changes in the Azores High that explain regional differences in arid/humid intervals. Gray dashed contours reflect the long-term mean SLP in the LME, color

contours various deviations in SLP that might occur. Dots indicate locations of proxy records from BG cave, Spain stalagmites, and Morocco stalagmites



at 2° horizontal resolution and available for the period 1871–2012 (Compo et al. 2011), and the National Centers for Environmental Prediction (NCEP) and NCAR Reanalysis (NNR) at 2.5° horizontal resolution and available for the period 1948-present (Kistler et al. 2001). The common analysis period for validation between LME and the SLP products was taken as 1950–2005.

4 Results

4.1 Environmental monitoring

The suitability of BG for paleoclimate reconstruction relies on generally stable conditions in cave atmosphere. In situ monitoring of BG demonstrates that the cave atmosphere remained at or near 100% relative humidity throughout the study period (August 2013–March 2022) while cave temperature varied little ($<\pm1.0$ °C) on an annual basis and closely reflected regional mean average temperature. Barometric pressure inside the cave also varied little (Fig. S1; Thatcher et al. 2020a). The highest drip rates in the cave occurred, albeit slightly lagged, with continued precipitation during the wet season while lower drip rates correspond with drier summer conditions (Fig. S1; Thatcher et al. 2020a). These data illustrate a highly stable cave environment.

4.2 Age model

Ages were assigned to individual carbon isotope measurements using age models constructed from eighteen dates for BG136, seven dates for BG134, and five dates for BG131 (Table 1). Age uncertainties averaged 144 years (2σ) in these clean (low detrital Th), low uranium samples. The age model from BG136 was projected to 2013 CE based on the active growth occurring at the stalagmite top when the stalagmite was collected, and by a radiocarbon measurement (F modern = 1.0086 ± 0.0023 ; Table S1) at the top indicating the speleothem has grown since the mid-twentieth century atmospheric ¹⁴C anomaly ("bomb peak"). Age models for BG131, BG134, and the portion of BG136 (BG136b) before the hiatus were developed using U-Th dates and uncertainties using iscam and supported by COPRA and StalAge (Fig. 3).

The uncertainties from U-Th dating (average of \pm 144 years at 2 s.d.) did not allow tight chronological control and thus we used fluorescent laminae in stalagmite BG136 to develop a more robust age model for the portion of the stalagmite that grew after the climatically-driven hiatus (the top ~ 24 mm of BG136; Fig. 4). An age model for the portion of the BG136 (BG136a) that has was deposited

following the hiatus was developed using laminae counting and compared with U-Th estimates (Fig. 3).

Initial counts were performed by measuring distances of 10-year counts of laminae (Fig. S3). From counts of 10-year bins of laminae, growth rates have varied substantially over entire record with a decrease in growth rates since the hiatus (Fig. S3). A total of five laminae counts and measurements were performed on the section since the hiatus in BG136 (Fig. 3). The median count, which was used in creation of the age model for BG136a, is 738 (range 715–797) years since the end of the hiatus (~1275 CE). This agrees well with the U-Th-based estimate of number of years since the hiatus and thus supports the annual nature of these laminae (Fig. 3).

After careful consideration of all possible age models and due to the interest in generating a composite record, the final age model used to construct the time series presented in Fig. 5 was developed using iscam from the U-Th ages and laminae counts on BG136 and U-Th ages only on BG131 and BG134. StalAge and COPRA age models were used to verify the validity of the iscam age mode. Similarity between the three age models is robust as demonstrated in Fig. 3.

4.3 Carbon isotopic values

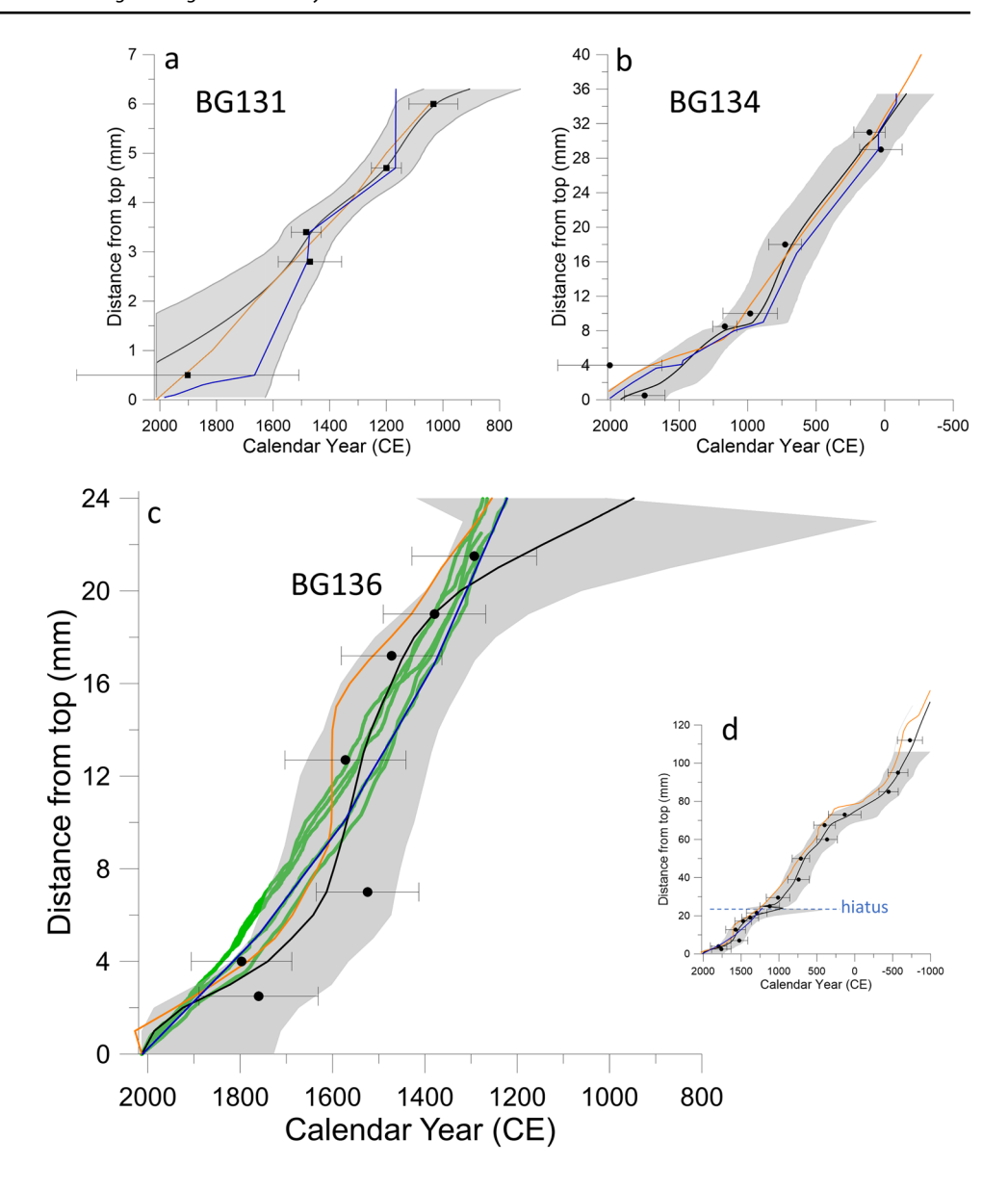
Carbon isotope data from the four portions of the three stalagmites (BG131, BG134 and BG136 above (BG136a) and below (BG136b) the hiatus) were combined into one composite record using iscam. Correlations (R²) for overlapping sections were 0.72, 0.85, and 0.83 (all p<0.05), respectively. The presence of a hiatus in BG136 as indicated by a drastic change in isotope values as well as a textural change in the calcite made BG136 difficult to use for climate interpretations alone. Since BG134 did not appear to have a hiatus, pairing the stalagmites using iscam allowed for a complete climate history from BG cave over the last 1200 years.

The BG composite carbon isotope record is presented in Fig. 5 and each data point incorporated an average of 2.3 ± 1.9 years. The carbon isotope record presented in Fig. 5a shows the isotopic values for each stalagmite presented as a composite record (lighter green) as well as the results from a low pass filter (bolder green, passband = 0.075) of carbon isotopes. There was an offset in isotopes between the stalagmites (see Fig. 5b and Fig. S4) and the filtered data allowed for the main climate signal and variability greater than annual scale to emerge. These values were then z-scored before being compared with the z-scores of other regional hydroclimate records in Fig. 10.

Carbon isotope values in the ~1200 years since 800 CE reveal substantial decadal to multidecadal variability with some centennial scale trends (Fig. 5a). The data illustrate six prominent stages within the last 1200 years: (1) sustained



Fig. 3 Age models for BG stalagmites. a BG131; b BG134; c BG136 above hiatus; d BG136 above and below hiatus through 3000 yrs BP. StalAge-derived (orange), COPRA-derived (black), and iscam-derived (blue) age models for individual stalagmites from Buraca Gloriosa. Black circles are U-Th dates with 2σ errors. Gray shading indicates the 95% confidence interval from COPRA. See Table 1 for specific ages and isotopic ratios. c Also includes five laminae counts (green) which were used as an additional age model constraint



high δ^{13} C values with only minor variability from 800 to 1200 CE; (2) a marked (within about 50 years) decrease between 1200 and 1250 CE, after which δ^{13} C values seem to define a new baseline; (3) decadal scale variability with centennial scale variability from 1250 to 1600 CE; (4) increased δ^{13} C values centered around 1600 CE with a return to lower values by ~1650 CE; (5) a gradual increase in δ^{13} C values from 1650 CE into the Modern/Industrial era; and (6) a decrease in carbon isotope values in the uncorrected data since ~1880 CE and a continuation of the increase from (5) in the Suess-corrected data.

4.4 Community Earth System Model (CESM1)

To understand changes in the atmospheric circulation over the North Atlantic region, we assessed attributes of the AH since 850 CE using the Last Millennium Ensemble (LME) simulations. In the long-term mean SLP, the AH and Icelandic Low are the dominant features across the region; in the zonal mean SLP across the North Atlantic sector, these two locations also exhibit pronounced interannual variability (Fig. S5). The LME skillfully represents the overall structure and variability in North Atlantic SLP, compared to a range of observational products in the twentieth century (Supplemental Information; Fig. S6). Our main focus here is on the AH, given its relation to Iberian hydroclimate, specifically event analyses of the AH. This approach acknowledges that variability exists across a range of timescales and looks for winters with extreme attributes and changes in the frequencies of these attributes. This approach does not simply look at whether long-term mean AH conditions were higher or lower than average during certain periods.

The LME captures changes in intensity, size, and location of the wintertime (DJF) AH during the last 1200 years. The



Fig. 4 Annual fluorescent laminae in BG136. The bright green lines running left to right are cracks in the stalagmite

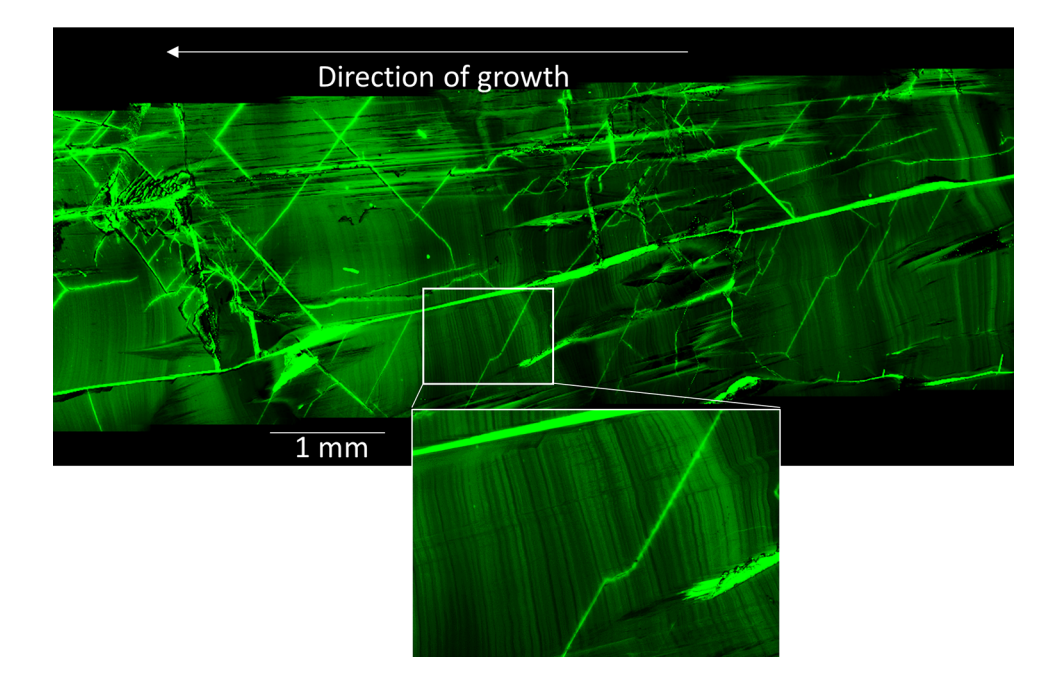
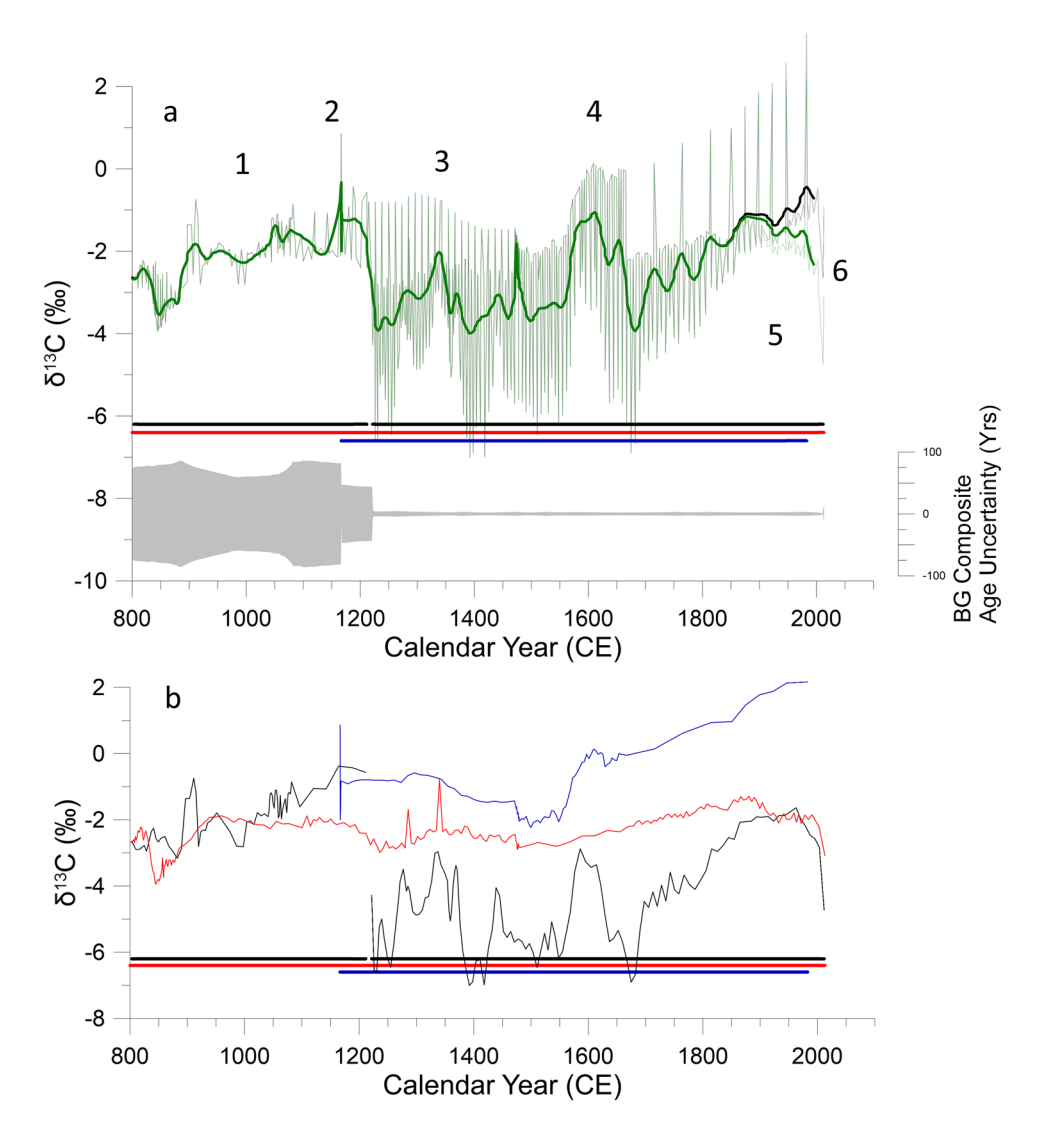


Fig. 5 BG carbon isotope record. a Lighter green is BG Composite record and bolder green is the low pass (0.075) filtered data. Numbers indicate the time periods discussed in 4.3. Black line indicates isotope values for stalagmite record that have been corrected for the Suess Effect with the bolder black line indicating the low pass filtered data. Plot at the bottom indicates the uncertainty (in years) in the BG Composite carbon isotope record over the past 1200 years. b Individual carbon isotope records—black (BG136), red (BG134), and blue (BG131). Bars at the bottom of the plot indicate years of each stalagmite record. Note the short hiatus in BG136 at ~CE





number of winters exhibiting AH conditions that fall within the extreme 10% of each attribute (e.g. large, small, strong, weak, north, south, east, or west) has been plotted as a frequency per 100 years in Figs. 6, 7, 8 and 9 (subplot e). These data are not suggesting that there was a continuous extreme

AH attribute (extreme eastern position, for example) but rather that the frequency of winters with extremely eastern AH position, for example, was increased or reduced during certain periods. A number of interesting features emerge with these data. For each extreme attribute (for example,

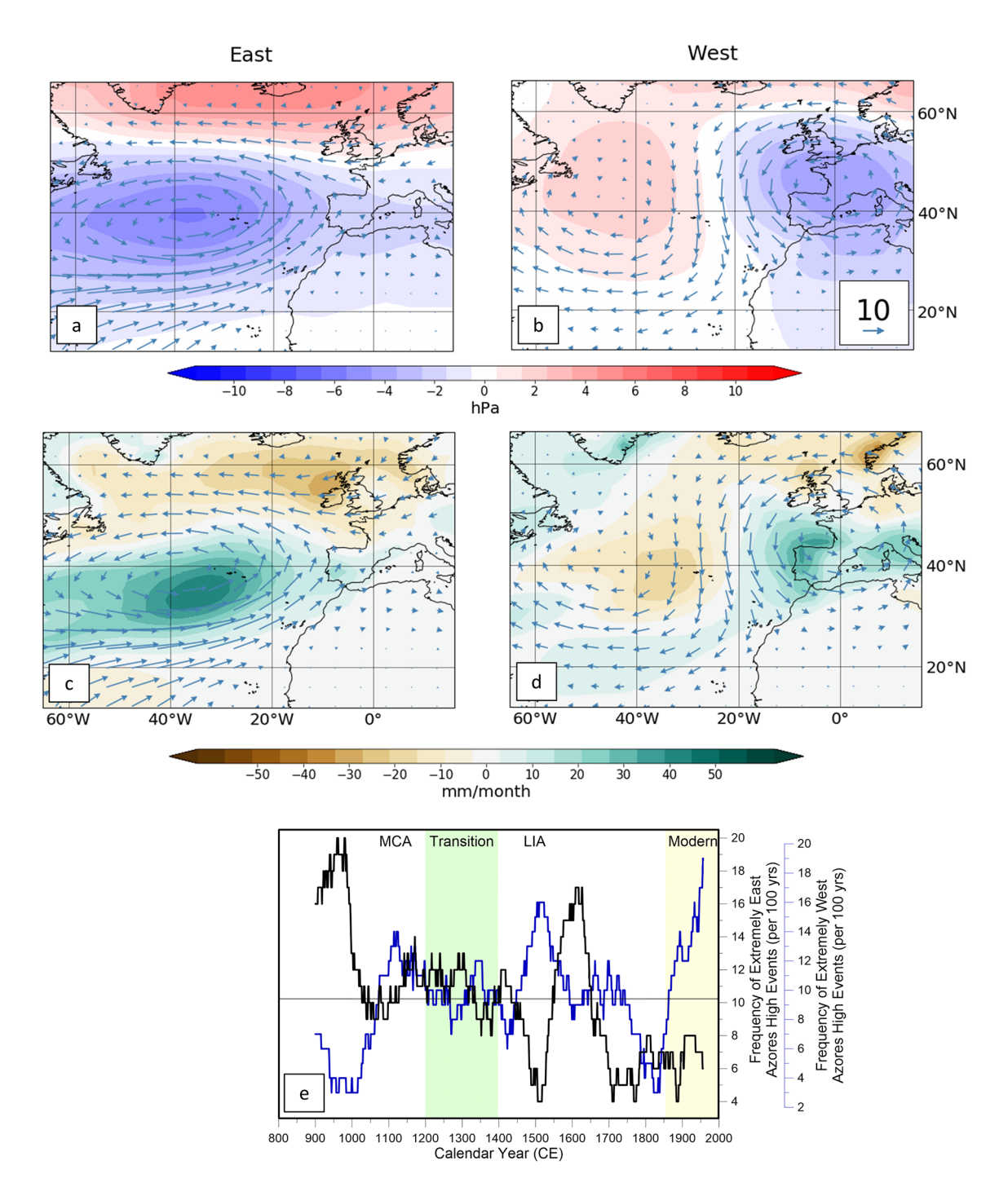


Fig. 6 Hydroclimate during winters with extremely eastern and western Azores High positions and their frequency of occurrence in the climate model simulations. Composite anomalies of **a**, **b** sea level pressure (red-blue contours) and moisture transport in g/kg*m/s (vectors) and **c**, **d** precipitation (brown-green contours) and mois-

ture transport (vectors) during winters with extremely east and west Azores High. Anomaly patterns were calculated using the Last Millennium Ensemble. e Extreme west (blue) and extreme east (black). Average frequency per 100 years is shown (black horizontal line)



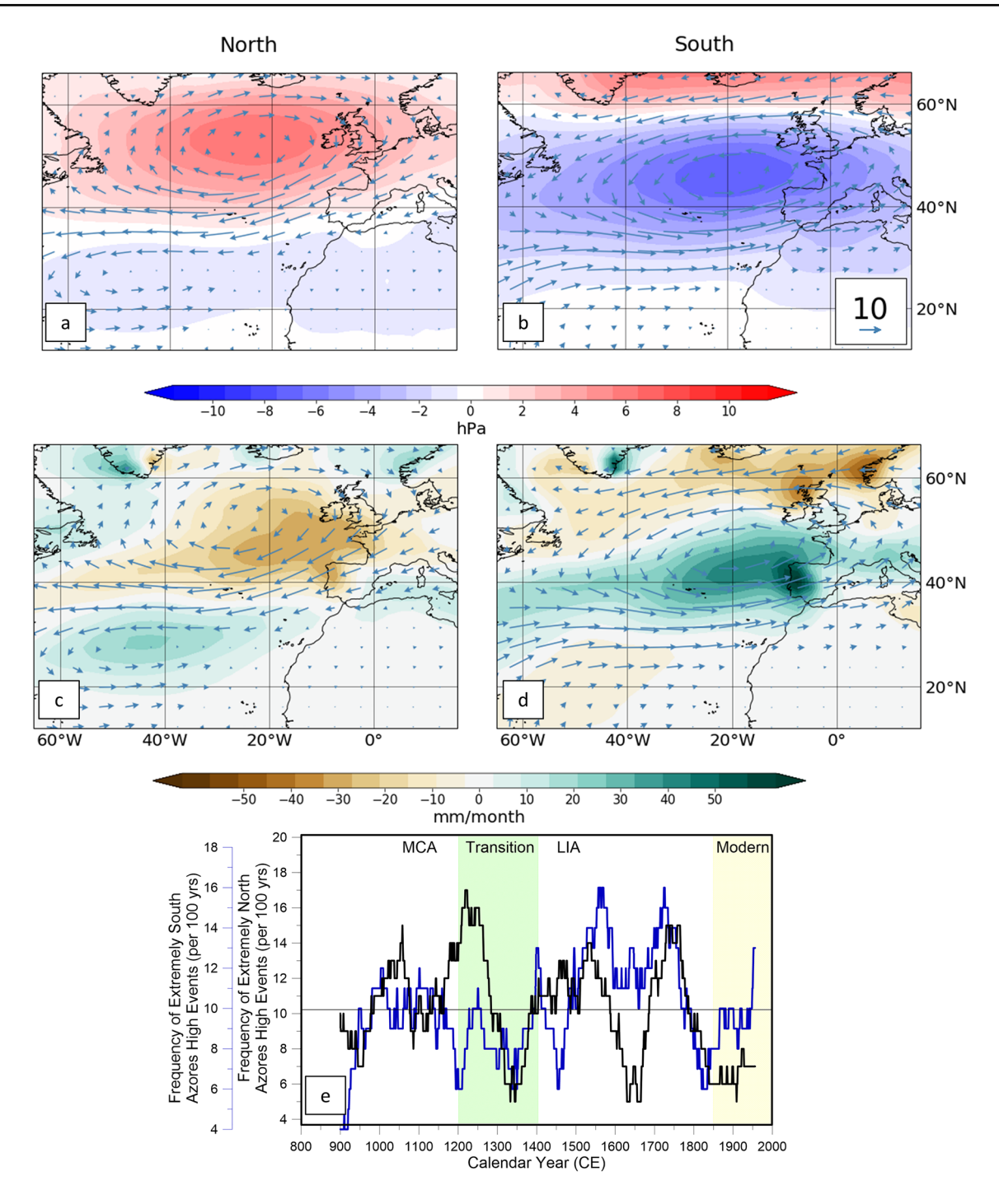


Fig. 7 Hydroclimate during winters with extremely northern and southern Azores High positions and their frequency of occurrence in the climate model simulations. Composite anomalies in **a**, **b** sea level pressure (red-blue contours) and moisture transport in g/kg*m/s (vectors) and **c**, **d** precipitation (brown-green contours) and moisture

transport (vectors) during winters with extremely north and south Azores High. Anomaly patterns were calculated using the Last Millennium Ensemble. **e** Extreme north (black) and extreme south (blue). Average frequency per 100 years is shown (black horizontal line)

extremely north position or extremely strong intensity), associated pressure, moisture transport, and wintertime precipitation anomalies have been calculated for the North Atlantic region (Figs. 6, 7, 8 and 9, subplots a–d).

During winters with an extremely eastern position of the AH, pressure anomalies are slightly lower than the long-term average for western Iberia, moisture transport anomalies are from the southwest off of the Atlantic, and



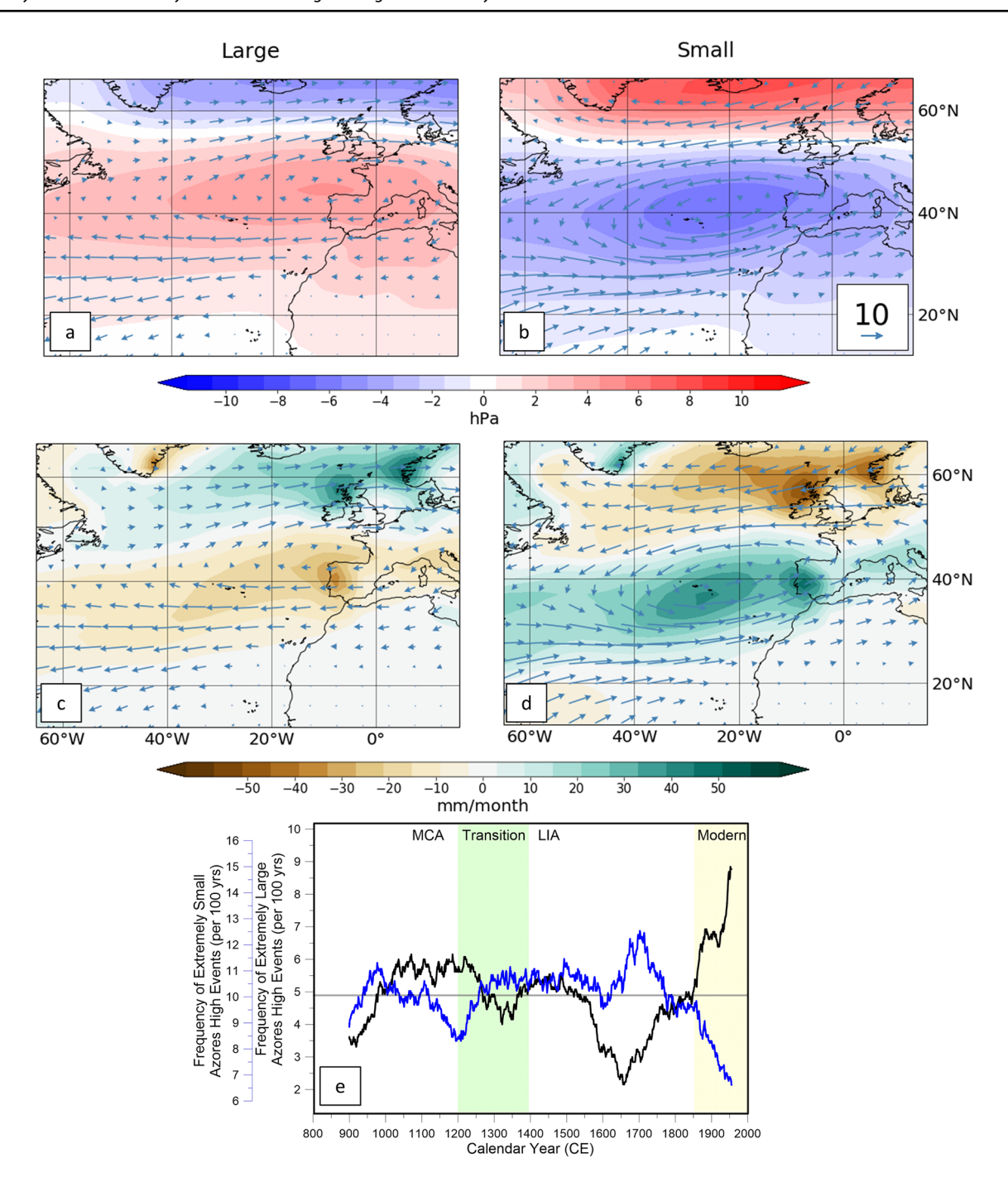


Fig. 8 Hydroclimate during winters with extremely large and small Azores High and their frequency of occurrence in the climate model simulations. Composite anomalies in **a**, **b** sea level pressure (red-blue contours) and moisture transport in g/kg*m/s (vectors) **c**, **d** precipitation (brown-green contours) and moisture transport (vectors) dur-

ing winters with extremely large and small Azores High. Anomaly patterns were calculated using the Last Millennium Ensemble. e Extreme large (black) and extreme small (blue). Average frequency per 100 years is shown (black horizontal line). Adapted from Cresswell-Clay et al. (2022)

precipitation anomalies are slightly higher for western Iberia (wetter than average) (Fig. 6a and c). For the winters with the extremely western position, pressure anomalies are negative, moisture transport anomalies are more northerly, and precipitation anomalies indicate much wetter than average conditions (Fig. 6b and d).

Prior to 1000 CE, there were very few winters with an extremely western position of the AH (Fig. 6e) and a



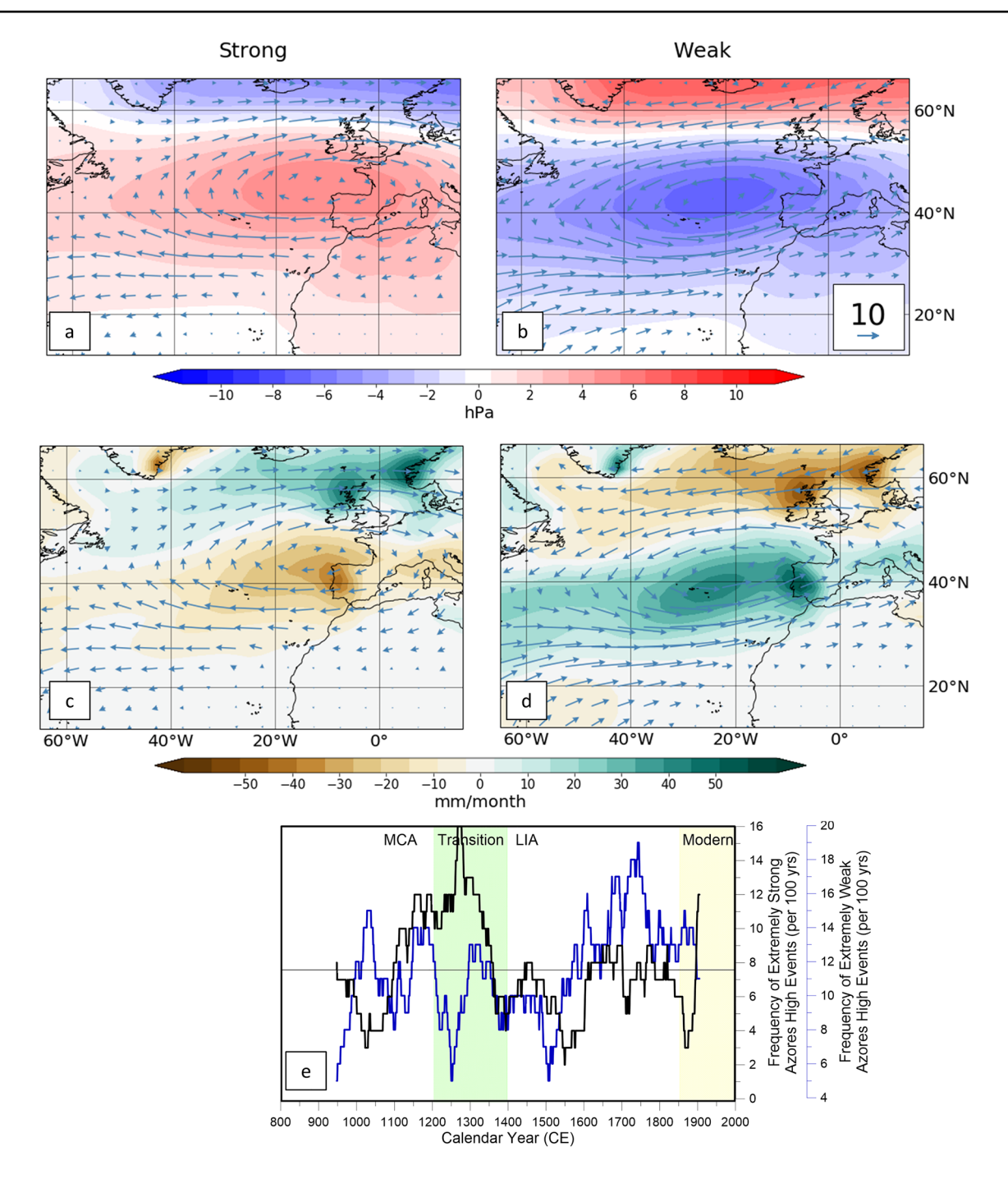


Fig. 9 Hydroclimate during winters with extremely strong and weak Azores High and their frequency of occurrence in the climate model simulations. Composite anomalies in **a**, **b** sea level pressure (red-blue contours) and moisture transport in g/kg*m/s (vectors) and **c**, **d** precipitation (brown-green contours) and moisture transport (vectors)

during winters with extremely strong and weak Azores High. Anomaly patterns were calculated using the Last Millennium. e Extreme weak (black) and extreme strong (blue). Average frequency per 100 years is shown (black horizontal line)

larger frequency of winters with extremely east positions, then from about 1050 CE until about 1450 CE, there were equal numbers of extremely west and east positions. The frequency of winters with an extremely western position peaked at about 1500 CE, coincident with a decrease in the

frequency of winters with extreme eastern position. The frequency of extremely eastern positions peaked ~ 1600 CE and have remained less frequent since, while the frequency of extremely western positions have increased towards the end of the record.



During winters with an increased frequency of an extremely northern position of the AH, pressure anomalies are positive in western Iberia, moisture transport anomalies are off of the Iberian peninsula, indicative of reduced onshore moisture transport, and lower precipitation is indicated (Fig. 7a and c). The opposite is indicated in western Iberia for winters with an extremely southward AH position where pressure anomalies are negative, moisture transport anomalies are more Atlantic-based and anomalous wet conditions dominate (Fig. 7b and d).

Two peaks in the frequency of extreme northern positions (Fig. 7e) occurred early in the record—one at ~1050 CE and a larger one shortly after 1200 CE. After this larger peak, the frequency of northern positions drops to a low point by ~1350 CE. Another low point in the northern extremes is from 1600 to 1650 CE rising by 1750 CE to another peak before falling towards present day. The most notable features of the southern extremes are the dual peaks at ~1550 CE and ~1700 CE and above average frequency of winters with extreme southern positions from ~1400–1800 CE.

During winters with an increased frequency of an extremely large spatial coverage of the AH, pressure anomalies are positive, moisture transport anomalies are from the east (Iberia), indicative of reduced moisture onshore transport, and precipitation is substantially reduced in Portugal (Fig. 8a and c). Conversely, during winters with extremely small spatial coverage of the AH, pressure anomalies are negative, moisture transport anomalies from the Atlantic Ocean are enhanced, and precipitation is substantially increased in western Portugal (Fig. 8b and d).

The frequency of winters with extremely small spatial coverage of the AH decreases from ~950 CE to ~1200 CE and then rises toward a sustained higher frequency from ~1250 CE to ~1600 CE before peaking at ~1700 CE (Fig. 8e). After ~1700 CE, the frequency of winters with extremely small spatial coverage of the AH drops to the lowest levels over the entire simulated period. The frequency of winters with extremely large spatial coverage of the AH increases at the start of the record with sustained higher frequency from ~1000 to ~1250 CE. After a dip and another period of sustained slightly higher frequency, the frequency of extremely large spatial coverage of the AH declines to its lowest point in the record at 1650 CE before secularly increasing in frequency until present (Cresswell-Clay et al. 2022).

Periods of extremely strong intensity of the AH in Portugal are associated with positive SLP anomalies, moisture transport anomalies from the Iberian Peninsula, indicative of a reduction of onshore moisture transport from the Atlantic, and a substantial reduction in precipitation in Portugal (Fig. 9a and c). For winters with an extremely weak intensity of the AH, decreases in pressure, and enhanced moisture

transport from the WSW (Atlantic) and increases in precipitation are the main features in Portugal (Fig. 9b and d).

The frequency of winters with extremely strong intensity and weak intensity indicates enhanced AH variability since 900 CE. The frequency of winters with extremely strong AH intensity peaks from ~1100–1150 CE while frequency of winters with extremely weak intensity also reach a maximum soon after (~1250 CE). There is an increase in frequency of extreme weak intensity AH and a reduction in the frequency of extreme strong intensity AH 1650–1750 CE.

5 Discussion

5.1 Environmental controls on BG stalagmite δ^{13} C variability

Carbon isotopic values in speleothem carbonate are linked to a wide array of equilibrium and disequilibrium processes (Baker et al. 1997; Dorale et al. 1992; Genty et al. 2003; Hellstrom et al. 1998; Hendy 1971; Kong 2005; Mickler et al. 2004). Changes in precipitation influence vegetation (modern values above BG range from $\delta^{13}C_{\text{veg}} - 26.5$ to - 29.0%; Denniston et al. 2018; Thatcher et al. 2020b) abundance above BG. As demonstrated by Thatcher et al. (2020b) and Chen et al. (2020), especially in arid and semiarid regions like western Portugal, vegetation exhibits a high correlation with precipitation anomalies (i.e. higher precipitation = more vegetation) with a relatively short lag time between precipitation and vegetation response (1–2 months). In turn, these changes in vegetation drive shifts in carbon isotopic values of soil water, with δ^{13} C values increasing during drier periods that reflect reductions in soil density/ respiration resulting in a higher percentage of atmospheric CO_2 inputs with a pre-Industrial $\delta^{13}C$ value of approximately -6.4% (Francey et al. 1999). Additionally, during dry intervals, enhanced water-rock interaction (average BG bedrock $\delta^{13}C_{\text{rock}}$ value of $3.1 \pm 1.0\%$; Denniston et al. 2018) and/or outgassing of CO2 in voids above the cave leads to higher δ^{13} C values in residual solution due to prior calcite precipitation (Baker et al. 1997). Using vegetation and bedrock end member δ^{13} C values, carbon isotopes were demonstrated to be inversely proportional to mean wintertime rainfall (Thatcher et al. 2020b).

Variability in stalagmite carbon isotope values indicate changes in hydroclimate in western Portugal. Progressing into the MCA, there is an increase of carbon isotopes signaling drier conditions (leading to reduced vegetation density and interaction of vegetation and water) as the $\delta^{13}C$ isotopes primarily reflect the $\delta^{13}C$ value of the carbonate rock (Fig. 5a and b). Wetter conditions during the start of the LIA are also suggested by lower $\delta^{13}C$ values reflective of increased vegetation density and higher soil respiration rates



(see Genty et al. 2003). Drier conditions in Portugal since 1650 CE are evidenced by higher values of carbon isotopes.

Since ~ 1880 CE, carbon isotope values from the BG composite steadily decreased towards the present, potentially in response to the rise in atmospheric CO_2 derived (Suess Effect) from burning of fossil fuels, which have nominal $\delta^{13}C$ values around -27% (e.g., Sharp 2007). The black line in Fig. 5 indicates potential stalagmite carbon isotope values if the Suess Effect was not impacting this record. As is evident in this figure, accounting for anthropogenic emissions results in the continuation in the centuries-long trend toward increasing stalagmite $\delta^{13}C$ values.

5.2 Comparison with regional records

Integrating well-dated and high-resolution hydroclimate proxy records from Iberia and northwestern Africa will help facilitate the construction of a regional analysis of effective precipitation variability during the last 1200 years. Numerous studies have focused on past climate in the Iberian Peninsula/northwest Africa region through the use of lake and ocean sediment cores (Moreno et al. 2012), riverine discharge (Trigo et al. 2004), pollen spectra (Desprat et al. 2003) and marsh sediment chemistry (Moreno et al. 2015). However, in order to construct a regional depiction of hydroclimate, we selected only time series that were sampled at high-resolution (at least decadal), had strong chronological control, overlapped substantially with our records for the past 1200 years, and were sensitive to precipitation dynamics. This selection yielded four regional records that we compared to the BG multi-proxy record: a Spanish stalagmite carbon isotope record (Martín-Chivelet et al, 2011), Moroccan tree-ring record (Esper et al. 2007; Wassenburg et al. 2013), Moroccan stalagmite trace element record (Wassenburg et al. 2013), and Moroccan stalagmite δ^{18} O record (Ait Brahim et al. 2018). We also include nine NAO reconstructions (Fig. 10). To facilitate comparison, the BG composite stalagmite record and the four regional records are presented as z-scores, where $z = [(sample-mean)/\sigma])$.

The northernmost of these records is a composite stalagmite time series from three caves in northern Spain (Kaite Cave, Cuevo del Cobre, Cuevo Mayor; Fig. 1). Martín-Chivelet et al. (2011) presented a 4000-year combined $\delta^{13}C$ record from stalagmites in which the $\delta^{13}C$ record was presented as a temperature proxy. The authors suggested a relatively warm interval during the MCA and cooler period during the LIA, although others have argued that it was more likely related to a combination of factors such as hydroclimate variability than temperature variability alone (Domínguez-Villar 2011). The BG and Spanish $\delta^{13}C$ records are broadly coherent, particularly since 800 CE ($r^2 = 0.23$, p < 0.05; binned in 50-year windows with no age adjustments to either record). At BG, hydroclimate variability is

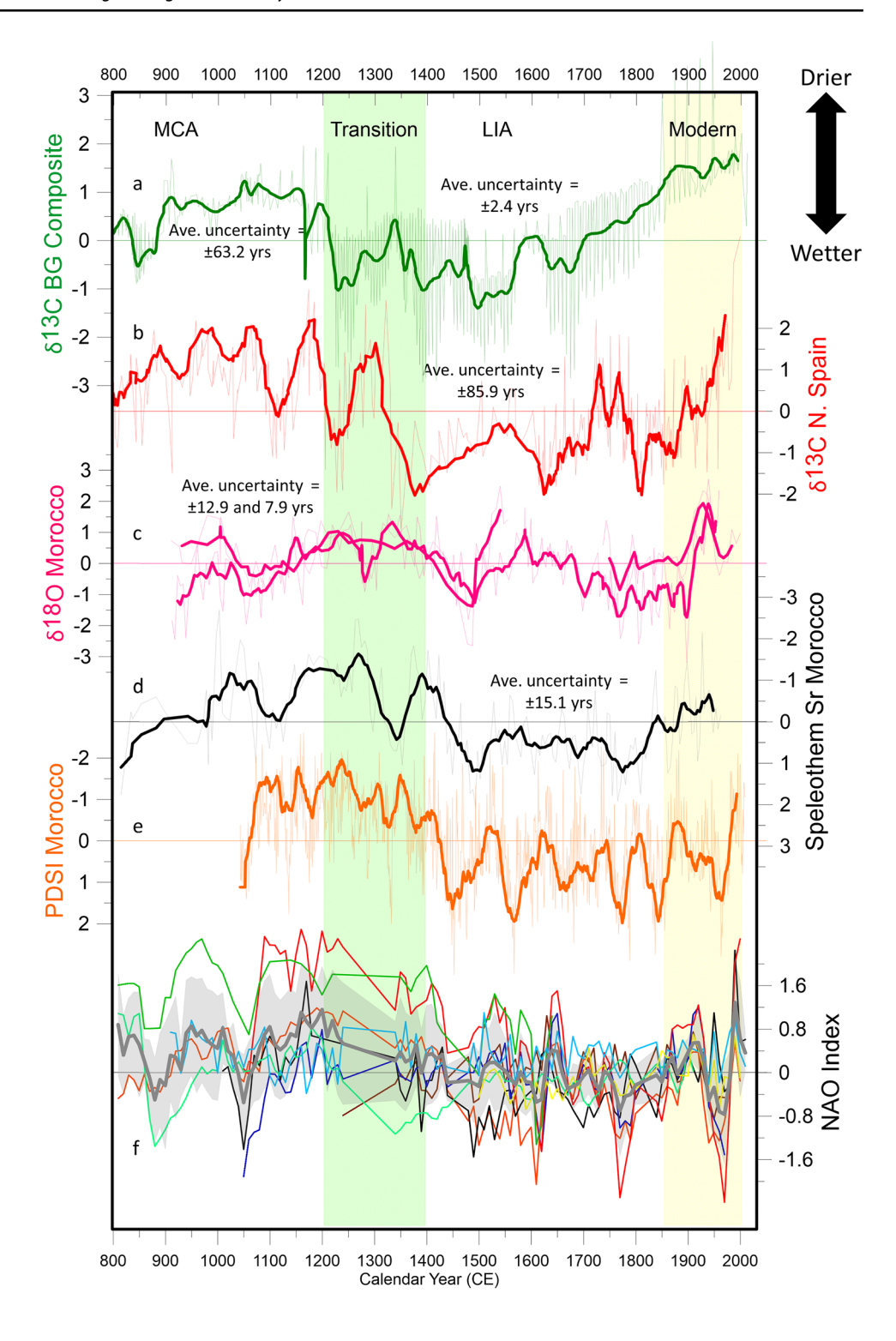
linked to vegetation abundance above the cave (Thatcher et al. 2020b). Enhanced precipitation increases vegetation density and thus δ^{13} C values primarily reflect those of the vegetation during pluvial periods while during drier episodes the δ^{13} C values shift to reflect those of the rock above the cave and stronger influences of prior calcite precipitation. Similar processes may be at work in the Spanish cave systems as well. We suggest that the δ^{13} C values in the Spanish record (Fig. 10) are consistent with inferred changes in hydroclimate as argued by Domínguez-Villar (2011). The Spanish carbon isotope record shows three distinct hydroclimate patterns during the MCA, LIA, and Modern era, similar in timing and magnitude to those from BG. Mean δ^{13} C values for the Spanish records are: $+0.7 \pm 0.9\%$ (MCA, defined here as 800-1250 CE); $-0.4 \pm 1.0\%$ (LIA, defined here as 1250-1850 CE), and $+0.2 \pm 1.3\%$ (Modern era, defined here as 1850 CE-present). Although the timing of the shift toward wetter conditions occurs slightly out of phase with BG, the Spanish record shows a distinct change in carbon isotope values beginning around 1300 CE. Some of the discrepancy between these records may be due to age uncertainties: ±86 years over the 1200 years for Spanish time series, and \pm 63 years for BG prior to 1220 CE and ± 2.4 years after 1220 CE (based on lamina counting). For the Spanish and BG record prior to 1220 CE, the average uncertainties were calculated using the average of U-Th errors over each time period.

Wassenburg et al. (2013) used a tree-ring width time series updated from that of Esper et al. (2007) from the Atlas Mountains, Morocco, and a stalagmite trace element record (Mg/Ca and Sr/Ca) from Grotte de Piste, from the northwestern part of the Middle Atlas Mountains to reconstruct effective rainfall in Morocco from 619 to 1962 CE (Fig. 10). The average age uncertainties in the Moroccan trace element records are smaller—15.1 years over the last 1200 years. The results from this study indicate that the MCA was dominated by conditions more arid than the LIA and thus likely related to positive NAO conditions. However, the study also revealed substantial wet intervals during the MCA. The Middle Atlas speleothem trace element data show secular decreases in Sr/Ca and increases in Mg/Ca during the MCA, indicative of reductions in precipitation over this time. During the thirteenth century, both the Moroccan tree ring and stalagmite records reveal a sharp change to wetter conditions (higher Sr, lower Mg) followed by a short recovery and then a return to wetter conditions during the late 14th and early fifteenth centuries. A clear trend towards drier conditions persists from 1760 to 1900 CE. These results are broadly consistent with the BG record (Fig. 10).

Other records from this region indicate potentially important forcing mechanisms, such as solar forcing and/ or NAO behavior. Ait Brahim et al. (2018) used stalagmite δ^{18} O records from the same cave as the Wassenburg et al.



Fig. 10 Comparison of BG δ^{13} C record with regional records. Comparison of Portugal hydroclimate record a δ¹³C (green) BG Composite record (Suess-corrected) with: **b** temperature reconstruction based on δ^{13} C (red) from three caves in northern Spain from Martín-Chivelet et al. (2011); c Morocco stalagmite δ¹⁸O from Ait Brahim et al. (2018); d Morocco stalagmite Sr/Ca ratio (ppm) (black) from Wassenburg et al. (2013); e Morocco tree ring (orange) drought reconstruction (PDSI) from Esper et al. (2007) and Wassenburg et al. (2013); f Nine individual NAO reconstructions (colored lines; as presented in Hernández et al. 2020) plus average and 2σ standard deviation (gray thick line and shading; Baker et al. 2015; Cook et al. 2019; Faust et al. 2016; Hernández et al. 2020; Luterbacher et al. 2001; Olsen et al. 2012; Ortega et al. 2015; Sjolte et al. 2018; Trouet et al. 2009). Modern Climate indicated by the yellow box and a transition period, indicated by green box, between MCA and LIA conditions. Stalagmite Sr/ Ca and PDSI records inverted such that down (up) indicates wetter (drier) conditions for panels (a-e). Records (a-d) are presented as z-scores. Average uncertainties are the average of U-Th errors over the last 1200 years

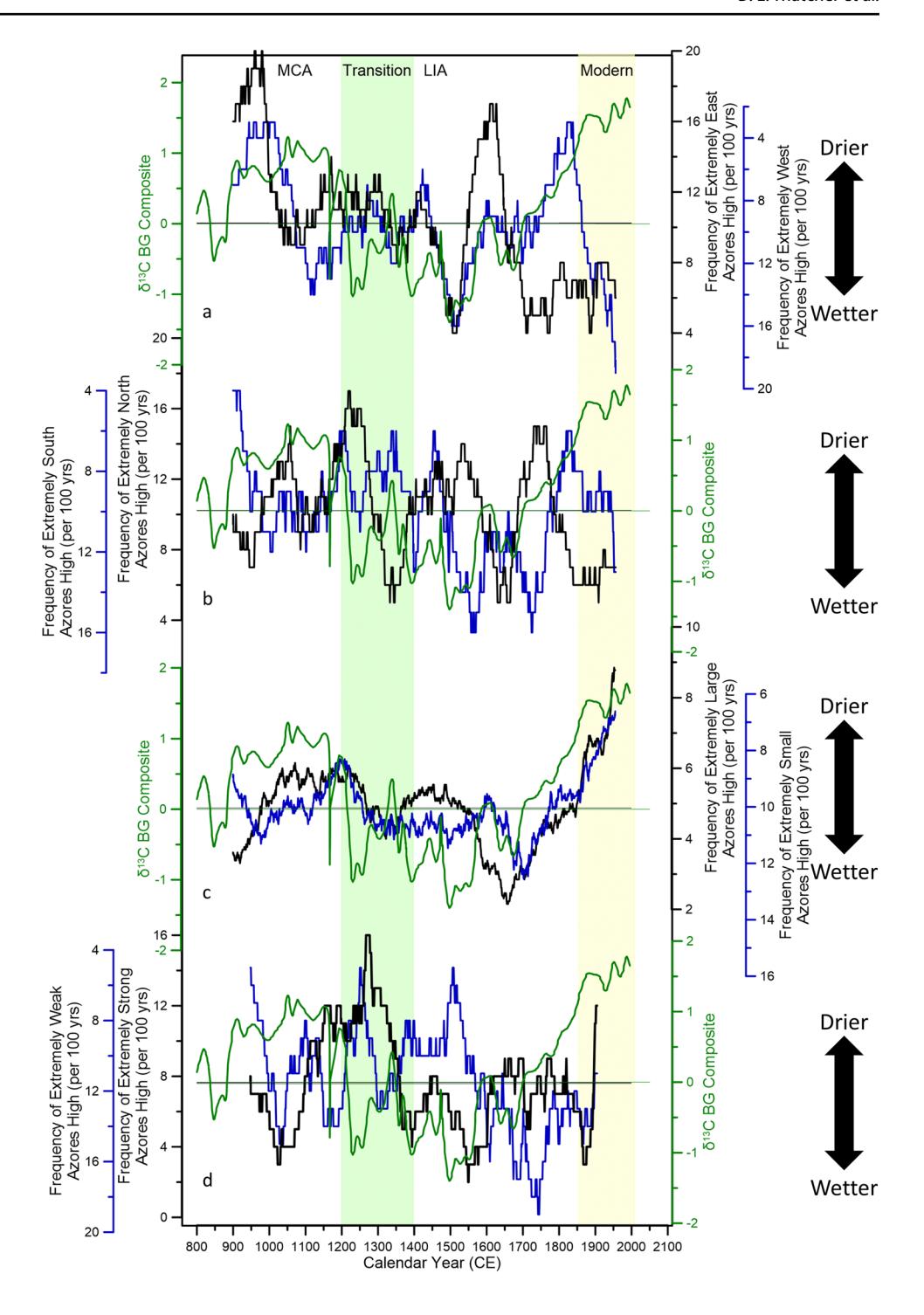


(2013) record plus a new location within 100 m of Grotte de Piste (Chaara cave) in Morocco to create a composite δ^{18} O record spanning the last 1000 years (Fig. 10). Age uncertainties in these stalagmite records from Grotte de Piste and Chaara cave are also small (12.9 and 7.9 years, respectively). Low values of δ^{18} O in this composite record correspond with NAO- phases and well-known

solar minima periods (Ait Brahim et al. 2018). Generally increasing values of $\delta^{18}O$ are prominent leading to a peak at ~ 1350 CE with a dip in this trend centered about 1300 CE. The time period 1400–1900 CE is wetter than other time periods with only drier conditions evident centered around 1600 CE. The authors found that, generally, negative NAO conditions and solar minima correspond to lower



Fig. 11 Time series of extreme Azores High events compared to the BG Composite δ^{13} C record. Black and blue lines are the same as shown in Figs. 6, 7, 8 and 9 with the blue line axes reversed. BG composite record (green) is shown in all plots for comparison. a Frequency of extremely north (black) and south (blue); b Frequency of extremely east (black) and west (blue); c Frequency of extremely large (black) and small (blue); d Frequency of extremely strong (black) and weak (blue)



values of $\delta^{18}\text{O}$ from these Moroccan stalagmites throughout the last 1000 years.

These four regional, precipitation-sensitive proxy records and nine NAO reconstructions reveal largely coherent patterns in rainfall variations over the past 1200 years including distinct climatic conditions during the MCA, LIA, and Modern Era (Fig. 10). A notable exception is the delayed onset of the MCA/LIA transition in northwest Africa relative

to Spain and Portugal, and this offset may reveal insights on regional hydroclimate variability.

If the changes in hydroclimate were primarily due to a shift in the *location* of the AH rather than simply a change in the *intensity* of the AH (and the NAO system), then we might expect to see a difference in the timing of this transition along a north to south transect. For example, the onset of LIA-enhanced precipitation began in Iberia prior to Morocco, indicating that the AH system shifted south at



this time, steering more Atlantic storms to the north, while blocking storms from reaching northwest Africa. Thus, the regional records (Fig. 10) likely illustrate a weakening of the AH into the LIA, but the transition period may have involved both a weakening and a southward migration of the AH. This interpretation may explain why the NAO reconstruction (Fig. 10) developed by Trouet et al. (2009) shows a weakening of the NAO (and, by inference, a weakening of the AH) after 1400 CE.

5.3 Changes in Azores High dynamics

It is difficult to determine the cause of an increase or decrease in SLP by assessing changes at a particular location. For example, from the study location at BG, if a SLP increase and decrease in precipitation is suggested by increased $\delta^{13}C$ values, it could be the result of a northward shift, an eastward shift, a strengthening, and/or an increase in AH size. The analyses performed with LME output allow for a critical attribution of changes in the BG carbon isotope record to various changes in behavior of the Azores High.

Changes in AH behavior have the potential to impact changes in precipitation across the Iberian Peninsula and northwest Africa. The changes evident in these regional precipitation-sensitive proxies could have varied temporally due to changes in AH position, size, and/or strength. In Fig. 11, some of the axes have been inverted relative to those shown in Figs. 6, 7, 8 and 9 so that AH behavior that corresponds with drying conditions (as indicated by the LME climate model simulations shown in Figs. 6, 7, 8 and 9, subplots a and b) at BG are up.

During the MCA, (~850–1250 CE), there are several increases in frequency of winters with an extremely northern position (Fig. 11a), a higher frequency of winters with extremely eastern position of the AH (Fig. 11b) at the start, an increase in the frequency of winters with extremely large spatial coverage throughout the MCA (Fig. 11c), and an increase in the frequency of winters with extremely strong AH intensity (Fig. 11d) as the MCA progresses, all of which would contribute to aridity in this region.

A sudden decrease in the BG composite record is evident near 1200–1250 CE. Accompanying this carbon isotope shift are an increase in the frequency of extremely southern positions and an increase in frequency of weak intensity AH attributes (Fig. 11b and d). The BG record has some of the lowest values of isotopes during the last 1200 years indicating wet conditions in western Portugal. Progressing through the next century, there is a decrease in the frequency of northern positions but no change in the frequency of extremely southern positions, indicating that the general motion of the AH over this important transition period is from north to south. As mentioned above, this southward shift may explain the differences in timing

between the earlier transition in the BG and Spain records and the later transition in the Morocco records from the dry MCA conditions to wetter LIA.

The most sustained wet period in the last 1200 years in western Portugal is ~ 1250 CE until 1700 CE (generally LIA) with a small drying event in the early fourteenth century and a larger drying event centered at 1600 CE. The record of extremely small spatial coverage of the AH indicates a higher frequency during this LIA time period (Fig. 11c). Additionally, there are more extremely western positions (Fig. 11a), generally more extremely southern positions especially during the second half of the LIA (Fig. 11b), and fewer extremely strong intensity AH winters over much of the LIA (Fig. 11d).

The drying event in the BG record centered ~ 1600 CE follows a prolonged wet period in western Portugal and precedes another brief wetter interval. This arid interval coincides with a higher frequency of extremely eastern positions, much like the start of the MCA (Fig. 11).

During the time period 1650–1750 CE, there is a peak in extremely small spatial coverage of the AH and a substantial decline in the frequency of extremely large spatial coverage of the AH that coincides with a wet interval (1650–1700 CE) in the BG Composite record. The time series presented in Figs. 6, 7, 8, 9 and 11 are the frequency of winters with extreme attributes per 100 years, and thus the frequency record ends in 1956 CE in order to maintain a 100-year average through 2005 CE. From the late 1800s through the end of the record, there are noticeable increases in the frequency of winters with AH in extremely western positions or with extremely large spatial coverage, both of which are associated with drier conditions in western Portugal.

5.4 Implications for regional atmospheric dynamics

Many proxy records from coastal Atlantic Europe and northwest Africa provide substantial evidence of distinct hydroclimate regimes in the last millennium; however substantial debate regarding the spatiotemporal dynamics of hydroclimate, especially during the MCA, and the driving mechanisms responsible still remain. Based on the records discussed here, medieval times were largely dry, although likely more variable than noted by Trouet et al. (2009), in the Iberian Peninsula and northwest Africa compared to the more humid LIA interval. The behavior of the Icelandic Low and the AH, and thus the winter NAO system, likely exerted the most control on regional hydroclimates. Near the Iberian Peninsula and NW Africa, the distinct hydroclimatic patterns noted here (Fig. 10) during the MCA and the LIA were likely caused by changes in the behavior (intensity, size, and/or location) of the AH system. Climate model simulations (Fig. 7e) suggest that the mean position of the AH was further north during the MCA compared to the LIA and



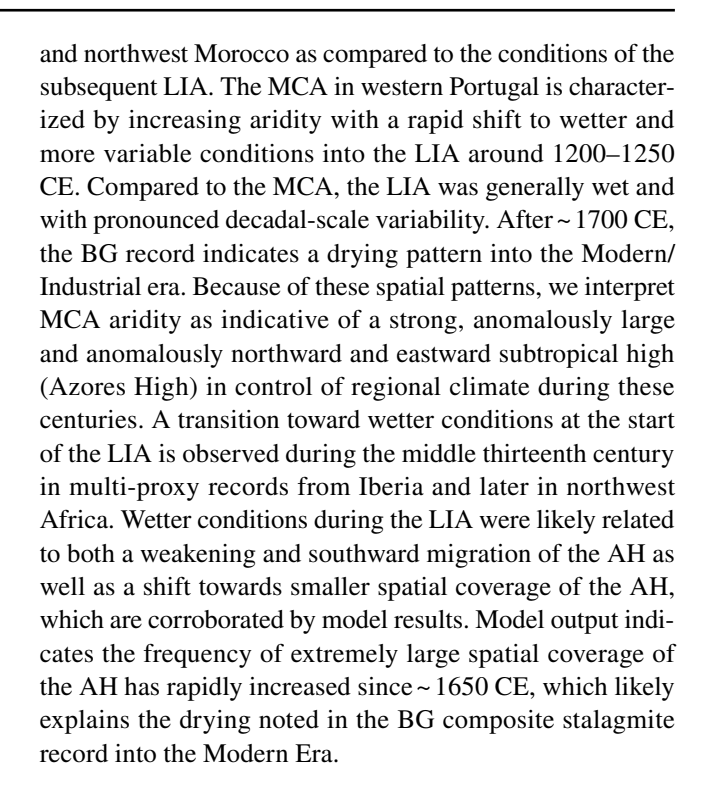
that there was a substantial weakening of the Azores High (decreased SLP) in the thirteenth and fourteenth centuries (Fig. 9e).

Although substantial uncertainty (± 15 –85 years) exists in the chronologies of several of the records, a major finding presented here indicates that Portugal became substantially wetter earlier than northwest Africa at the transition from the MCA into the LIA. This result is consistent with other precipitation sensitive records in Norway and Spain (Faust et al. 2016; Martín-Chivelet et al. 2011). A southward migration of the ITCZ during the transition time between MCA and LIA regimes and the concomitant shift in Hadley cell location is a potential explanation for the relative difference in timing between Iberia and Morocco, with Portugal becoming wetter earlier than Morocco (Thatcher et al. 2020a). A southward shift of the ITCZ could have corresponded with a concomitant shift in the descending limb of Hadley cell (Azores High). As demonstrated by Kang and Lu (2012), the poleward expansion of the Hadley cell coincides with shifts in the ITCZ in the summer hemisphere and throughout the year in climate model simulations under a warmer climate in the twenty-first century. This configuration may also be emblematic of the MCA. Changes in the Hadley cell circulation are important, yet not well understood, components of climate variability (Brönnimann et al. 2015).

The NAO reconstruction of Trouet et al. (2009) has received some criticism from the modeling community, in part because of the inability of climate models to reproduce an entrenched positive NAO for the MCA (e.g., Lehner et al. 2012; Ortega et al. 2015). However, our composite BG stalagmite record shares several important similarities to the Trouet et al. (2009) NAO reconstruction and contradicts these modeling results. The most important similarity is that medieval times in both the BG and the southern Trouet et al. (2009) record from Morocco were predominantly dry and drier than the LIA. However, unlike the Trouet et al. (2009) study, these regional proxy records all indicate only semipersistent atmospheric conditions and/or different timing for the persistent conditions, which likely involved an intense (or shifted) AH system (and a positive NAO index) that was punctuated by intervals of weakened AH conditions (and a negative NAO index) leading to periodic wet conditions in the MCA in some of the regional records. These discrepancies further illustrate the need for more proxy/modeling comparisons regarding the state of the AH and the NAO system during recent millennia.

6 Conclusions

The Buraca Gloriosa (BG) composite stalagmite record reveals relatively persistent dry conditions during the MCA, consistent with reconstructions for northern Spain



Supplementary Information The online version contains supplementary material available at https://doi.org/10.1007/s00382-022-06427-6.

Acknowledgements We thank Pedro Ribeiro, Jace Bricker, Alaina Chormann, Gabi Hiatt, Amanda Houts, Mark Mathison, Madelyn Mette, Steve Rasin, Hannah Thatcher, and Jayna Wanamaker for help with field work and logistics. ADW was supported by National Science Foundation (NSF) grant 1804528, CCU by NSF grant 1804132, the Ocean Climate Change Institute and James E. and Barbara V. Moltz Fellowship for Climate-Related Research at WHOI, RFD by the Center for Global and Regional Environmental Research, NSF grant 1804635, and Cornell College, YA and VP by NSF grant 1806025, DPG by NSF grant 1805163, and JAH by NSF grants BCS-0455145, BCS-0612923, and BCS-1118155. We thank the CESM Paleoclimate Working Group for running and making available the model output for the CESM1 (CAM5) Last Millennium Ensemble Community Project and acknowledge supercomputing resources provided by NSF/CISL/Yellowstone. NCEP-NCAR reanalysis, HadSLP2r, 20th Century Reanalysis provided by NOAA/OAR/ESRL PSD, Boulder, Colorado, through their website http://www.cdc.noaa.gov/psd, and supported by the U.S. Department of Energy, Office of Science Innovative and Novel Computational Impact on Theory and Experiment program, and Office of Biological and Environmental Research, and by the NOAA Climate Program Office. Thanks to Natalie Renier (WHOI Graphics) for help with the design of Fig. 2. Sampling performed under the auspices of IGESPAR (to JAH) and Associação de Estudos Subterrâneos e Defesa do Ambiente. Comments by two anonymous reviewers on an earlier version of the manuscript are gratefully acknowledged.

Author contributions All authors contributed to the study conception and design. Fieldwork was performed by DLT, ADW, RFD, JH, DPG. Material preparation, data collection and analysis were performed by DLT, ADW, RFD, CCU, NC, VJP, YA. The first draft of the manuscript was written by DLT and ADW and all authors commented on previous versions of the manuscript. All authors read and approved the final manuscript.



Funding The author(s) disclosed receipt of the following financial support for the research, authorship, and/or publication of this article: This work was supported, in part, by NSF grant 1804528 (ADW), NSF grant 1804132 (CCU), the Center for Global and Regional Environmental Research and NSF grant 1804635 (RFD), NSF grant 1806025 (YA and VP), NSF grant 1805163 (DPG), and NSF grants BCS-0455145, BCS-0612923, and BCS-1118155 (JAH), and the Ocean Climate Change Institute and *James E. and Barbara V. Moltz Fellowship for Climate-Related Research* at WHOI (CCU).

Availability of data and material Stable and U-series isotope data are available at the NOAA National Centers for Environmental Information website.

Code availability None.

Declarations

Conflict of interest None.

References

- Ait Brahim YA, Cheng H, Sifeddin A, Wassenburg JA, Cruz FW, Khodr M, Sha L, Pérez-Zanón N, Beraaouz EH, Apaéstegui J, Guyot J-L, Jochum KP, Bouchaou L (2017) Speleothem records decadal to multidecadal hydroclimate variations in southwestern Morocco during the last millennium. Earth Planet Sci Lett 476:1–10. https://doi.org/10.1016/j.epsl.2017.07.0450012-821X
- Ait Brahim YA, Wassenburg JA, Cruz FW, Sifeddine A, Scholz D, Bouchaou L, Dassié EP, Jochum KP, Edwards RL, Cheng H (2018) Multi-decadal to centennial hydroclimate variability and linkage to solar forcing in the Western Mediterranean during the last 1000 years. Sci Rep 8:17446. https://doi.org/10.1038/s41598-018-35498-x
- Allan RJ, Ansell TJ (2006) A new globally complete monthly historical mean sea level pressure data set (HadSLP2): 1850–2004. J Clim 19:5816–5842. https://doi.org/10.1175/JCL13937.1
- Asmerom Y, Polyak V, Burns S (2010) Variable winter moisture in the southwestern United States linked to rapid glacial climate shifts. Nat Geosci 3:114–117. https://doi.org/10.1038/NGEO7 54
- Asmerom Y, Baldini JUL, Prufer KM, Polyak VJ, Ridley HE, Aquino VV, Baldini LM, Breitenbach SFM, Macpherson CG, Kennett DJ (2020) Intertropical convergence zone variability in the Neotropics during the Common Era. Sci Adv. https://doi.org/10.1126/sciadv.aax3644
- Baker A, Ito W, Smart PL, McEwan RF (1997) Elevated and variable values in δ¹³C in speleothems in a British cave system. Chem Geo 136:263–270
- Baker A, Wilson R, Fairchild I, Franke J, Spotl C, Matte D, Trouet V, Fuller L (2011) High resolution δ^{18} O and δ^{13} C records climate from an annually laminated Scottish stalagmite and relationship with last millennium climate. Glob Planet Change 79:303–311
- Baker A, Hellstrom JC, Kelly BF, Mariethoz G, Trouet V (2015) A composite annual-resolution stalagmite record of North Atlantic climate over the last three millennia. Sci Rep 5:1–8. https://doi.org/10.1038/srep10307
- Barnston AG, Livezey RE (1987) Classification, seasonality, and persistence of low-frequency atmospheric circulation patterns. Mon Weather Rev 115:1083–1126

- Breitenbach SFM, Rehfeld K, Goswami B, Baldini JUL, Ridley HE, Kennett DJ, Prufer KM, Aquino VV, Asmerom Y, Polyak VJ, Cheng H, Kurths J, Marwan N (2012) COnstructing Proxy Records from Age Models (COPRA). Clim past 8:1765–1779
- Brönnimann S, Fischer AM, Rozanov E, Poli P, Comp GP, Sardeshmukh PD (2015) Southward sift of the northern tropical belt from 1945 to 1980. Nat Geosci 8:969–975
- Chen Z, Wang W, Fu J (2020) Vegetation response to precipitation anomalies under different climatic and biogeographical conditions in China. Sci Rep 10:830
- Cheng H, Edwards RL, Shen CC, Polyak VP, Asmerom Y, Woodhead J, Hellstrom J, Wang Y, Kong X, Spötl C, Wang X, Alexander EC (2013) Improvements in 230Th dating, 230Th and 234U half-life values, and U-Th isotopic measurements by multicollector inductively coupled plasma mass spectrometry. Earth Planet Sc Lett 371–372:82–91
- Collister C, Mattey D (2008) Controls on water drop volume at speleothem drip sites: an experimental study. J Hydrol 358:259–267
- Comas-Bru L, McDermott F (2014) Impacts of the EA and SCA patterns on the European twentieth century NAO-winter climate relationship. Q J R Meteorol Soc 140:354–363
- Compo GP, Whitaker JS, Sardeshmukh PD, Matsui N, Allan RJ, Yin X, Gleason BE, Vose RS, Rutledge G, Bessemoulin P, Brönnimann S, Brunet M, Crouthamel RI, Grant AN, Groisman PY, Jones PD, Kruk M, Kruger AC, Marshall GJ, Maugeri M, Mok HY, Nordli Ø, Ross TF, Trigo RM, Wang XL, Woodruff SD, Worley SJ (2011) The twentieth century reanalysis project. Q J Roy Meteorol Soc 137:1–28
- Cook ER, Seager R, Kushnir Y, Briffa KR, Buntgen U, Frank D, Krusic PJ, Tegel W, van der Schrier G, Andreu-Hayles L, Baillie M, Baittinger C, Bleicher N, Bonde N, Brown D, Carrer M, Cooper R, Cufar K, Dittmar C, Esper J, Griggs C, Gunnarson B, Gunther B, Gutierrez E, Haneca K, Helama S, Herzig F, Heussner K, Hofmann J, Janda P, Kontic R, Kose N, Kyncl T, Levanic T, Kinderholm H, Manning S, Melvin TM, Miles D, Neuwirth B, Nicolussi K, Nola P, Panayotov M, Popa I, Rothe A, Seftigen K, Seim A, Svarva H, Svoboda M, Thun T, Timonen M, Touchan R, Trotsiuk V, Trouet V, Walder F, Wazny T, Wilson R, Zang C (2015) Old World megadroughts and pluvials during the Common Era. Sci Adv 1:10. https://doi.org/10.1126/sciadv.1500561
- Cook ER, Kushnir Y, Smerdon JE, Williams AP, Anchukaitis KJ, Wahl ER (2019) A Euro-Mediterranean tree-ring reconstruction of the winter NAO index since 910 C.E. Clim Dyn. https://doi.org/10.1007/s00382-019-04696-2
- Cresswell-Clay N, Ummenhofer CC, Thatcher DL, Wanamaker AD, Denniston RD, Asmerom Y, Polyak VJ (2022) Unprecedented expansion of the azores high due to anthropogenic climate change. Nat Geosci. https://doi.org/10.1038/s41561-022-00971-w
- Davis RE, Hayden BP, Gay DA, Phillips WL, Jones GV (1997) The North Atlantic Subtropical Anticlone. J Clim 10:728–744
- Denniston RF, Houts AN, Asmerom Y, Wanamaker AD, Haws JA, Polyak VJ, Thatcher DL, Altan-Ochir S, Borowske AC, Breitenbach SFM, Ummenhofer CC, Regala FT, Benedetti MM, Bicho NF (2018) A stalagmite test of North Atlantic SST and Iberian hydroclimate linkages over the last two glacial cycles. Clim Past 14:1893–1913
- Desprat S, Goni MFS, Loutre M-F (2003) Revealing climatic variability of the last three millennia in northwestern Iberia using pollen influx data. Earth Planet Sci Lett 213:63–78
- Dominguez-Villar D (2011) Comment on "Land surface temperature changes in Northern Iberia since 4000 yr BP, based on δ^{13} C of speleothems." Glob Planet Change 100:291–294
- Dorale JA, Gonzalez LA, Reagan MK, Pickett DA, Murrell MT, Baker RG (1992) A high-resolution record of Holocene climate change



- in speleothem calcite from Cold Water Cave, northeast Iowa. Science 258:1626-1630
- Druffel EM, Benavides LM (1986) Input of excess CO2 to the surface ocean based on 13C/12C ratios in a banded Jamaican sclerosponge. Nature 321:58–61
- Esper J, Frank D, Buntgen U, Verstege A, Luterbacher J (2007) Longterm drought severity variations in Morocco. Geophys Res Lett 34:5
- Falarz M (2019) Azores High and Hawaiian High: correlations, trends and shifts (1948–2018). Theor App Climatol 138:417–431
- Faust JC, Fabian K, Milzer G, Giraudeau J, Knies J (2016) Norwegian fjord sediments reveal NAO related winter temperature and precipitation changes of the past 2800 years. Earth Planet Sci Lett 435:84–93
- Fohlmeister J (2012) A statistical approach to construct composite climate records of dated archives. Quat Geochronol 14:48–56
- Francey RJ, Allison CE, Etheridge DM, Trudinger CM, Enting IG, Leuenberger M, Langenfelds RL, Michel E, Steele LP (1999) A 1000-year high precision record of δ^{13} C in atmospheric CO₂. Tellus 51B:170–193
- Genty D, Blamart D, Ouahdi R, Gilmour M, Baker A, Jouzel J, Van-Exter S (2003) Precise dating of Dansgaard-Oeschger climate oscillations in western Europe from stalagmite data. Nature 421:833–837
- Griffiths ML, Kimbrough AK, Gagan MK, Drysdale RN, Cole JE, Johnson KR, Zhao J-X, Cook BI, Hellstrom JC, Hantoro WS (2016) Western Pacific hydroclimate linked to global climate variability over the past two millennia. Nat Commun 7:1–9
- Haug G, Hughen KA, Sigman DM, Peterson LC, Rohl U (2001) Southward Migration of the Intertropical Convergence Zone through the Holocene. Science 293:1304–1308
- Hellstrom JC, McCulloch MT, Stone J (1998) A 31,000 year highresolution record of southern hemisphere maritime changes, from the sable isotope geochemistry of New Zealand speleothems. Quat Res 50:167–178
- Hendy C (1971) The isotopic geochemistry of speleothems—I. The calculation of the effects of different modes of formation on the isotopic composition of speleothems and their applicability as palaeoclimatic indicators. Geochim Cosmochim Act 35:801–824
- Hernández A, Sánchez-López G, Pla-Rabes A, Comas-Bru L, Parnell A, Cahill N, Trigo RM, Giralt S (2020) A 2,000-year Bayesian NAO reconstruction from the Iberian Peninsula. Sci Rep 10:14961
- Hurrell J (1995) Decadal trends in the North Atlantic Oscillation: Regional temperatures and precipitation. Science 269:676–679
- IPCC (2013) Fifth Assessment Report (AR5), Climate Change 2013: The Physical Science Basis. Contribution of Work Group I to the Fifth Assessment Report of the Intergovernmental Panel on Climate Change, Cambridge Press, Cambridge, United Kingdom and New York, NY, USA. 1552 pp
- Iqbal MJ, Hameed S, Khan F (2013) Influence of Azores High pressure on Middle Eastern rainfall. Theor Appl Climatol 111:211–221
- Kang S, Lu J (2012) Expansion of the Hadley cell under global warming: winter versus summer. J Clim 25:8387–8393
- Karnauskas KB, Ummerhofer CC (2014) On the dynamics of the Hadley circulation and subtropical drying. Clim Dyn 42:2259–2269
- Keeling CD (1979) The Suess effect: ¹³Carbon-¹⁴Carbon interrelations. Environ Int 2:229–300
- Kistler R, Colllins W, Saha S, White G, Woollen J, Kalnay E, Chelliah M, Ebisuzaki W, Kanamitsu M, Kousky V, van den Dool H, Jenne R, Fiorino M (2001) The NCEP–NCAR 50–year reanalysis: monthly means CD–ROM and documentation. Bull Amer Meteor 82:247–267
- Kong X (2005) Complicated responses of stalagmite δ^{13} C to climate change during the last glaciation from Hulu Cave, Nanjing, China. Sci China Ser D 48:2174

- Lehner F, Raible C, Stocker T (2012) Testing the robustness of a precipitation proxy-based North Atlantic Oscillation reconstruction. Quat Sci Rev 45:85–94
- Lopez-Moreno JI, Vicente-Serrano SM (2008) Positive and negative phases of the wintertime North Atlantic Oscillation and drought occurrence over Europe: a multitemporal-scale approach. J Clim 21:1220–1243
- Luterbacher J, Xoplaki E, Dietrich D, Jones PD, Davies TD, Portis D, Gonzalez-Rouco JF, von Storch H, Gyalistras D, Casty C, Wanner H (2001) Extending North Atlantic Oscillation reconstructions back to 1500. Atmos Sci Lett 2:114–124
- Martín-Chivelet J, Munoz-Garcia MB, Edwards RL, Turrero MJ, Ortega AI (2011) Land surface temperature changes in Northern Iberia since 4000 yr BP, based on δ¹³C of speleothems. Global Planet Change 77:1–12
- Mickler PJ, Banner JL, Stern L, Asmerom Y, Edwards RL, Ito E (2004) Stable isotope variations in modern tropical speleothems: evaluating equilibrium vs kinetic isotope effects. Geochim Cosmochim Acta 68:438104393
- Moreno A, Morellon M, Martin-Puertas C, Frigola J, Canals M, Cacho I, Corella JP, Perez A, Belmonthe A, Vegas-Vilarrubia T, Gonzalez-Samperiz P, Valero-Garces BL (2011) Was there a common hydrological pattern in the Iberian Peninsula region during the Medieval Climate Anomaly? PAGES 1:16–17
- Moreno A, Perez A, Frigol J, Nieto-Morena V, Rodrigo-Gamiz M, Martrat B, Gonzalez-Samperiz P, Morellon M, Martin-Pertas C, Corella J, Belmonte A, Sancho C, Cacho I, Herrara G, Canals M, Grimalt JO, Jimenez-Espejo F, Martinez-Ruiz F, Vegas-Vilarrubia T, Valero-Garces BL (2012) The Medieval Climate Anomaly in the Iberian Peninsula reconstructed from marine and lake records. Quat Sci Rev 43:16–32. https://doi.org/10.1016/j.quascirev.2012.04.007
- Moreno J, Fatela F, Leorri E, Araujo MF, Moreno F, De La Rosa J, Freitas MC, Valente T, Corbett DR (2015) Bromine enrichment in marsh sediments as a marker of environmental changes driven by Grand Solar Minima and anthropogenic activity (Caminha, NW of Portugal). Sci Total Environ 506–507:554–566
- Olsen J, Anderson NJ, Knudsen MF (2012) Variability of the North Atlantic Oscillation over the past 5,200 years. Nat Geosci 5:808-812
- Ortega P, Lehner F, Swingedouw D, Masson-Delmotte V, Raible CC, Casado M, Yiou P (2015) A model-tested North Atlantic Oscillation reconstruction for the past millennium. Nature 523:71–74
- Otto-Bliesner B, Brady E, Fasullp J, Jahn A, Landrum L, Stevenson S, Rosenbloom N, Mai A, Strand G (2015) Climate variability and change since 850 C.E.: an ensemble approach with the community earth system model (CESM). Bull Amer Meteor Soc 97:735–754. https://doi.org/10.1175/BAMS-D-14-00233.1
- Proctor CJ, Baker A, Barnes WL, Gilmour MA (2000) A thousand year speleothem proxy record of North Atlantic climate from Scotland. Clim Dyn 16:815–820
- Raible CC, Lukusch U, Fraedrich K (2004) Precipitation and Northern Hemisphere regimes. Atmos Sci Lett 5:43–55
- Raible CC, Lehner F, Gonzalez-Rouco JF, Fernandez-Donado L (2014) Changing correlation structures of the Northern Hemisphere atmospheric circulation from 1000 to 2100 AD. Clim past 10:537–550
- Railsback LB, Brook GA, Liang F, Voarintsoa NRG, Cheng H, Edward RL (2018) A multi-proxy climate record from a northwestern Botswana stalagmite suggesting wetness late in the Little Ice Age (1810–1820 CE) and drying thereafter in response to changing migration of the tropical rain belt or ITCZ. Palaeogeogr Palaeoclimatol Palaeoecol 506:139–153
- Ramos-Román MJ, Jimenez-Moreno G, Anderson RS, Garcia-Alix A, Toney JL, Jimenez-Espejo FJ, Carrion JS (2016) Centennial-scale



- vegetation and North Atlantic Oscillation changes during the Late Holocene in the southern Iberia. Ouat Sci Rev 143:84–95
- Rashid SA, Iqbal MJ, Hussain MA (2012) Impact of north-south shift of azores high on summer precipitation over north west Europe. Int J Geosci 3:992–999
- Rodrigues M, Fonseca A (2010) Geoheritage assessment based on large-scale geomorphological mapping: contributes from a Portuguese limestone massif example. Geomorphologie Relief Processus Environnement 2:189–198
- Rüdisühli S, Sprenger M, Leutwyler D, Schär C, Wernli H (2020) Attribution of precipitation to cyclones and fronts over Europe in a kilometer-scale regional climate simulation. Weather Clim Dynam 1:675–699. https://doi.org/10.5194/wcd-1-675-2020
- Sanchez-Lopez G, Hernadez A, Pla-Rabes S, Trigo RM, Toro M, Granados I, Saez A, Masque P, Pueyo JJ, Rubio-Ingles MJ, Giralt S (2016) Climate reconstruction for the last two millennia in central Iberia: The role of East Atlantic (EA), North Atlantic Oscillation (NAO) and their interplay over the Iberian Peninsula. Quat Sci Rev 149:135–150
- Schmutz C, Luterbacher J, Gyalistras D, Xoplaki E, Wanner H (2000) Can we trust proxy-based NAO index reconstructions? Geophys Res Lett 27:1135–1138
- Schneider T, Bischoff T, Haug GH (2014) Migrations and dynamics of the intertropical convergence zone. Nature 513:45–53
- Scholz D, Hoffman DL (2011) StalAge—an algorithm designed for construction of speleothem age models. Quat Geochronol 6:369–382
- Schöne BR, Wanamaker AD Jr, Fiebig J, Thébault J, Kreutz K (2011)
 Annually resolved δ¹³C shell chronologies of long-lived bivalve
 mollusks (Arctica islandica) reveal oceanic carbon dynamics in
 the temperate North Atlantic during recent centuries. Palaeogeogr
 Palaeoclimatol Palaeoecol 302:31–42
- Seidel DJ, Fu Q, Randel WJ, Reichler TJ (2008) Widening of the tropical belt in a changing climate. Nat Geosci. https://doi.org/10.1038/ngeo.2007.1038
- Sharp Z (2007) Stable isotope geochemistry, New Jersey
- Sjolte J, Sturm C, Adolphi F, Vinther BM, Werner M, Lohmann G, Muscheler R (2018) Solar and volcanic forcing of North Atlantic climate inferred from a process-based reconstruction. Clim past 14:1179–1194
- Swart PK, Greer L, Rosenheim BE, Moses CS, Waite AJ, Winter A, Dodge RE, Helmle K (2010) The C-13 Suess effect in scleractinian corals mirror changes in the anthropogenic CO2 inventory of the surface oceans. Geophys Res Lett 37:L05604. https://doi.org/ 10.01029/02009GL041397
- Tandon N, Gerber E, Sobel A, Polvani L (2013) Understanding Hadley cell expansion versus contraction: insights from simplified models and implications for recent observations. J Clim 26:4304–4321
- Thatcher DL, Wanamaker AD, Denniston RD, Asmerom Y, Polyak V, Fullick D, Ummenhofer CC, Gillikin DP, Haws J (2020a) Hydroclimate variability from western Iberia (Portugal) during the Holocene—insights from a composite stalagmite isotope

- record. Holocene 30:966-981. https://doi.org/10.1177/09596 83620908648
- Thatcher DL, Wanamaker AD, Denniston RD, Ummenhofer CC, Regala FT, Jorge N, Haws J, Chorman A, Gillikin DP (2020b) Linking the karst record to atmospheric, precipitation, and vegetation dynamics in Portugal. Chem Geol 558:119949. https://doi.org/10.1016/j.chemgeo.2020.119949
- Trenberth KE, Paolino DA (1980) The Northern Hemisphere sea-level pressure data set: trends, errors, and discontinuities. Mon Weather Rev 108:855–872
- Trigo RM, Pozo-Vazquez D, Osborn TJ, Castro-Diez Y, Gamiz-Fortis S, Esteban-Parra MJ (2004) North Atlantic Oscillation influence on precipitation, river flow, and water resources in the Iberian Peninsula. Int J Climatol 24:925–944
- Trigo RM, Zêzere JL, Rodrigues ML, Trigo IF (2005) The influence of the North Atlantic Oscillation on rainfall triggering of landslides near Lisbon. Nat Hazards 36:331–354
- Trouet V, Esper J, Graham NE, Baker A, Scourse JD, Frank DC (2009) Persistent positive North Atlantic Oscillation mode dominated the Medieval climate anomaly. Science 324:78–80
- van Loon H, Rogers JC (1978) The seesaw in winter temperatures between Greenland and northern Europe. Part I: general description. Mon Weather Rev 106:296–310
- Verburg P (2007) The need to correct for the Suess effect in the application of the δ^{13} C in sediment of autotrophic Lake Tanganyika, as a productivity proxy in the Anthropocene. J Paleolimnol 37:591–602
- Wallace JM, Hobbs PV (2006) Atmospheric science: an introductory survey, Burlington
- Wassenburg JA, Immenhauser A, Richter DK, Niedermayr A, Riechelmann S, Fietzke J, Scholz D, Jochum KP, Fohlmeister J, Schroder-Ritzrau A, Sabaoui A, Riechelmann DFC, Schneider L, Esper J (2013) Moroccan speleothem and tree ring records suggest a variable positive state of the North Atlantic Oscillation during the Medieval Warm Period. Earth Planet Sci Lett 375:291–302. https://doi.org/10.1016/j.epsl.2013.05.048
- Wassenburg JA, Dietrich S, Fietzke J, Fohlmeister J, Jochum KP, Scholz D, Richter DK, Sabaoui A, Spötl C, Lohman G, Andreae MO, Immenhauser A (2016) Reorganization of the North Atlantic Oscillation during early Holocene deglaciation. Nat Geosci. https://doi.org/10.1038/NGEO2767

Publisher's Note Springer Nature remains neutral with regard to jurisdictional claims in published maps and institutional affiliations.

Springer Nature or its licensor holds exclusive rights to this article under a publishing agreement with the author(s) or other rightsholder(s); author self-archiving of the accepted manuscript version of this article is solely governed by the terms of such publishing agreement and applicable law.

